Geothermometric Constraints on the Thermal Architecture, Metamorphism, and Exhumation of the Northern Range, Trinidad

Published Version:
Gennaro, I., Weber, J., Vitale Brovarone, A., Arkle, J., Chu, X.u. (2022). Geothermometric Constraints on the Thermal Architecture, Metamorphism, and Exhumation of the Northern Range, Trinidad. JOURNAL OF METAMORPHIC GEOLOGY, 41, 1-23 [10.1111/jmg.12697].

Availability:
This version is available at: https://hdl.handle.net/11585/905011 since: 2023-03-01

Published:
DOI: http://doi.org/10.1111/jmg.12697

Gennaro, Ivano; Weber, John; Vitale Brovarone, Alberto; Arkle, Jeanette; Chu, Xu:
Geothermometric Constraints on the Thermal Architecture, Metamorphism, and Exhumation of the Northern Range, Trinidad

JOURNAL OF METAMORPHIC GEOLOGY vol. 41 ISSN 0263-4929

DOI: 10.1111/jmg.12697

Geothermometric Constraints on the Thermal Architecture, Metamorphism, and Exhumation of the Northern Range, Trinidad

Ivano Gennaro[1*†], John Weber[2], Alberto Vitale Brovarone[3, 4, 5], Jeanette Arkle[6], Xu Chu[1]

[1] Department of Earth Sciences, University of Toronto. Toronto, Ontario M5S 3B1, Canada
[2] Department of Geology, Grand Valley State University. Allendale, Michigan 49401, USA
[3] Dipartimento di Scienze Biologiche, Geologiche e Ambientali, Alma Mater Studiorum Università di Bologna, Bologna, Italy.
[4] Sorbonne Université, Museum National d'Histoire Naturelle, UMR CNRS 7590, IRD, Institut de Minéralogie, des Physique de Matériaux et de Cosmochimie, Paris, France
[5] Institute of Geosciences and Earth Resources, National Research Council of Italy, Pisa, Italy
[6] Department of Geology, Augustana College, Rock Island, IL 61201, USA

*Ivano Gennaro: ivanogennaro@gmail.com; https://orcid.org/0000-0002-9903-781X
John Weber: weberj@gvsu.edu
Alberto Vitale Brovarone: alberto.vitaleb@unibo.it
Jeanette Arkle: jennyarkle@augustana.edu; https://orcid.org/0000-0003-0640-6178
Xu Chu: xu.chu@utoronto.ca; https://orcid.org/0000-0002-6816-1076

† Current institute: Département de Sciences de la Terre, Université de Genève, 1205 Genève, Switzerland

Running Title

Thermal architecture of the Northern Range

Keywords

RSCM geothermometry, Trinidad, Geothermometry, Caribbean tectonics

Data Availability

The data presented here as supplemental material (Tables S1 and S2) are openly available on the PANGAEA Database and may be accessed under the DOI: https://doi.pangaea.de/10.1594/PANGAEA.932772

Abstract

The Northern Range of Trinidad is composed of Mesozoic passive margin sedimentary rocks that underwent ductile deformation and sub-greenschist to greenschist facies metamorphism in the early Miocene. Previous studies identified a westward increase in the metamorphic grade but were unable to resolve whether this trend was discrete or continuous. In this study, we use Raman spectroscopy on carbonaceous materials (RSCM) to constrain peak temperatures across the Northern Range with a greater resolution than was available in previous studies. These data are then combined with published thermochronological data to constrain the tectonic history of a range-cutting fault that had been previously inferred in previous geologic mapping. The RSCM temperatures show an abrupt increase from 337 ± 10 °C in the east to 442 ± 16 °C west of the Chupara Fault at Chupara Point. Our RSCM-derived peak metamorphic temperatures are 50–100 °C higher than those from previous estimates, requiring revision of tectonic models to account for deeper burial and greater exhumation. The peak metamorphic conditions determined here, and our inferred timing of faulting, are consistent with the two-stage tectonic model proposed in previous studies. A two-sided wedge formed during oblique plate collision and mountain building (stage I). Cooling rates differed in the Northern Range between eastern and western blocks between ~10–4.5 Ma; this difference is attributed here to the activity along the cross-range Chupara Fault. This pattern of differential cooling, bedrock exhumation, and inferred bedrock and surface uplift may be associated with plate-scale strike-slip tectonics and the passage of a crustal-scale bulge induced by deep tearing of South American lithosphere (stage II).

1. INTRODUCTION

Trinidad, the largest island in the nation of Trinidad and Tobago, is the southeastern-most island in the Caribbean and is located in the Caribbean-South American plate boundary zone (Fig. 1a), where the Caribbean plate currently moves east relative to the South American Plate at a rate of ~20 mm/yr (Weber, Dixon, et al., 2001). Current dextral plate motion is accommodated primarily along the Central Range Fault, which strikes NEE-SWW through the middle of the island (Weber, 2009; Weber, Dixon, et al., 2001). The Northern Range, composed of Mesozoic passive margin sedimentary rocks that were metamorphosed in the early Neogene, exposes pre-transform tectonic structures. Plate convergence in the early Miocene gave rise to shortening in the foreland fold-and-thrust belt and metamorphism at sub-greenschist to greenschist facies conditions in the Northern Range segment of the hinterland belt (Algar & Pindell, 1993; Frey et al., 1988; Weber, Ferrill, et al., 2001). Following the culmination of contraction and burial, exhumation of the hinterland metamorphic rocks took place from the Miocene to Pliocene, which is thought to have resulted from an oblique Caribbean-South American Plate collision (Algar & Pindell, 1993; Weber, Ferrill et al., 2001) and/or propagation of a deep-seated lithospheric tear fault (Arkle et al., 2017, 2021; Clark et al., 2008). The post-peak-metamorphic structures of the Northern Range preserve the history of the regional exhumation kinematics (Weber, Ferrill et al., 2001), but the general low grade of the Northern Range rocks limits the utility of conventional geothermometers for accurately assessing metamorphic conditions and changes. Illite crystallinity measurements, carbonate thermometry, muscovite-paragonite geothermometry, and mineral equilibria were used to establish baseline metamorphic conditions (Frey et al., 1988; Weber, Ferrill, et al., 2001). Using temperature-sensitive quartz and calcite microstructures, Weber, Ferrill, et al. (2001) were the first to recognize a systematic increase in deformation temperatures from east to west. However, this method involved high uncertainties in temperature estimates, making it difficult to identify whether this temperature gradient is continuous or segmented by discrete structures.

Raman spectroscopy on carbonaceous material (RSCM) is applicable to a wide range of lithologies within metamorphic terranes; it is particularly powerful in resolving low-grade peak metamorphic temperatures, such as those in the Northern Range. This geothermometric technique utilizes the crystallinity of carbonaceous material (CM) within the temperature range of 150–650 °C (Aoya et al., 2010; Beyssac et al., 2002; Kouketsu et al., 2014; Lahfid et al., 2010). With increasing metamorphic temperatures, amorphous CM evolves towards turbostratic carbon and then graphitic carbon through the process of graphitization, which is reflected in the relative areas of graphite and defect bands in Raman spectra (Beyssac & Lazzeri, 2012; Beyssac et al., 2002; Lahfid et al., 2010; Wopenka & Pasteris, 1993). Because graphitization is theorized to be an irreversible process, the crystallinity and Raman spectra of the CM should record peak metamorphic temperature conditions (Beyssac & Lazzeri, 2012; Beyssac et al., 2003). It is important to ensure quality sample collection and preparation for RSCM analysis, as for example, brittle deformation can affect the CM structure and therefore the calculated metamorphic temperatures (Nakamura et al., 2015; Kirlova et al., 2018). When high-resolution RSCM is combined with a high sample density this geothermometer can identify structural features not seen using less accurate methods (e.g., see Fig. 3 of Vitale Brovarone & Agard, 2013). The technique has been applied in a variety of metamorphic environments, from high-pressure terranes to contact aureoles (Bayet et al., 2018; Beyssac et al., 2019; Lahfid et al., 2010; Molli et al., 2018; Rahl et al., 2005; Simoes et al., 2007; Vitale Brovarone & Agard, 2013; Vitale Brovarone et al., 2013).

The Northern Range rocks and structures are deeply weathered, covered by dense tropical vegetation, and, aside from excellent coastal and stream exposures, are generally poorly exposed and difficult to access. Thus, previous structural studies have produced contradicting maps and interpretations (see below). In this study, we approach some of the unsolved structural and kinematic problems from a metamorphic perspective. Specifically, we use RSCM geothermometry to determine the peak metamorphic temperatures for a robust suite of Northern Range samples from east to west across the range (Fig. 2). We aimed to resolve the field gradient and to provide new temperature constraints to better establish the thermal architecture of the Northern Range. These new constraints help us determine whether the Northern Range was exhumed as a single rigid block or as discrete, fault-bounded range segments. Our new RSCM data, combined with previously published geological maps and thermochronological data, confirm the presence of a large-scale, cross-range, crustal-scale fault, the Chupara Fault, which was previously mapped but only poorly defined. Based on our new RSCM constraints, we review and modify existing tectonic models to explain the metamorphic, emplacement, and exhumation history of the Northern Range. The results presented here explore the thermal architecture and tectonic evolution of a mountain range formed in plate boundary that transitioned from collisional to transform, providing a real-world laboratory to examine processes that can then be used to better constrain geodynamic models (e.g. Govers & Wortel, 2005).

2. TECTONIC FRAMEWORK AND GEOLOGIC HISTORY

The Caribbean plate is postulated to have developed from the Caribbean large igneous province, an oceanic plateau or hotspot swell that formed from 139–83 Ma far west of its current location (Burke, 1988; Hoernle et al., 2004). The Caribbean plate began migrating eastward and entered the gap between the North and South American plates near the end of the Cretaceous (~66 Ma), and it eventually collided with northwestern South America (Kennan & Pindell, 2009) and southern North America. The rocks of the Northern Range were presumably derived from passive margin sediments deposited along the northern edge of South America (Frey et al., 1988; Robertson & Burke, 1989). These sedimentary rocks underwent low-grade metamorphism, with sub-greenschist mineral assemblages present in the east and greenschist assemblages present in the central and western Northern Range (Frey et al., 1988, Weber, Ferrill, et al., 2001). The presence of slates, marbles, quartzite and schists, as well as their detrital zircon U-Pb age spectra, supports a passive margin provenance for these rocks (Bartlett et al., 2021).

Zircon fission-track thermochronology data was used to suggest that the initial phase of metamorphism and deformation in the Northern Range may have started as early as the late Eocene (Algar & Pindell, 1993), but this interpretation was based on partially reset samples and from only a limited portion of the range. Subsequent studies used apatite fission track and apatite and zircon (U-Th)/He data to revealed that the initial exhumation of the Northern Range occurred ~10–8 Ma in west and ~6–4 Ma in the east (Arkle et al., 2021). Hinterland structural and metamorphic events are most clearly delineated in the western Northern Range. White mica $^{40}Ar/^{39}Ar$ ages date peak metamorphism in the Northern Range between 23 Ma and 34 Ma (Foland et al., 1992; Speed et al., 1997; Weber & Arkle, 2015). Syn-metamorphic deformation (isoclinal F_1 folding, transposition of original bedding, and S_1 foliation development) was followed by a second F_2 folding event and the development of S_2 crenulation cleavage (Weber, Ferrill, et al., 2001). The general picture is that plate-scale transpression drove high magnitude crustal shortening and exhumation in the southern Caribbean metamorphic hinterland, which includes the Northern Range (Cruz et al., 2007; Weber, Ferrill, et al., 2001). The main stages of deformation and exhumation in the hinterland belt are largely coeval with folding and thrusting in the Trinidad foreland, i.e., the Central and Southern Ranges. Deformation and exhumation in the Central Range is constrained to have occurred in the mid-Miocene (11–18 Ma) by using stratigraphy and zircon (U-Th)/He dating (Giorgis et al., 2017).

A late stage of deformation (D_3) within the Northern Range is recorded as a series of steeply dipping normal faults that strike SE-NW and NE-SW and crosscut previous fabric elements (Fig. 2; Kugler, 1961; Weber, Ferrill, et al., 2001). These faults have been interpreted as related to E-W transform shear, and as such, these faults may accommodate transtension associated with relative Caribbean-South American strike-slip motion (Algar & Pindel, 1993). Thus, Flinch et al. (1999) posit that these D_3 faults formed during or after the late Miocene or Pliocene.

Many different scenarios have been proposed to explain the metamorphism and exhumation of the metamorphic hinterland belt along northern South America. A few works advocate for the oblique collision and subduction of South America beneath the Caribbean plate (Audemard, 2009; Cruz et al., 2007; Pindell & Kennan, 2001, 2007, 2009). Some oblique collision models require about 240 km of displacement since 12 Ma to bring the Northern Range into its current position (Pindell & Kennan, 2001). Exhumation of the Northern Range has been explained by isostatic rebound after forming a deep crustal root that developed during an oblique collision (Algar & Pindell, 1993; Algar et al., 1998; Cruz et al., 2007), or through the activation of late-stage, range-bounding brittle structures. Weber, Ferrill, et al. (2001), for instance, initially called on differential dip-slip along the Arima Fault, a late south-side-down normal fault bounding the southern Northern Range (Fig. 1b & 2), to explain differences in eastern and western metamorphic grades.

Alternatively, metamorphism, deformation, and exhumation of the Northern Range could be associated with the passage of a lithospheric tear fault under Trinidad (Arkle et al., 2017, 2021; Clark et al., 2008; Levander et al., 2014). Currently, the subduction of the Atlantic oceanic lithosphere (of both the North and South American plates) under the Caribbean plate is accommodated by tearing of the lithosphere along a subduction-transform edge propagator (STEP, Fig. 1c; Govers and Wortel, 2005). STEP faults mark the transition between subduction and transform plate boundaries and are characterized by non-uniform relative plate motion; deformation, rotation, and uplift are often induced along the transform side of the transition as the subducting plate is torn at the STEP edge (Govers & Wortel, 2005). The active southeastern Caribbean STEP fault is marked by the Paria cluster of depth earthquakes beneath the northern coast of eastern Venezuela (Fig. 1a), and the active STEP edge is currently proposed to be positioned offshore eastern Trinidad, about 175 km east of the Paria cluster (c.f. Fig. 2 of Nijholt & Govers, 2015). Some recent interpretations have postulated that exhumation of the Northern Range was driven by STEP fault processes including the detachment of the South American lithosphere, asthenosphere flow, and flexural bulging ahead of the STEP tear (Arkle et al., 2017; 2021; Clark et al., 2008; Levander et al., 2014). Accordingly, eastward propagation of the Caribbean plate and associated STEP fault caused the observed asymmetric exhumation, and the thermochronological ages from the region that increase eastward and post-date the presumed oblique collision (Arkle et al., 2021). STEP-induced deformation also fits the observed Quaternary tectonic inversion and asymmetry of slow eastern and fast western exhumation rates (Arkle et al., 2017; Clark et al., 2008; Levander et al., 2014). Differences between regional tectonic models germane to this study are whether the hinterland metamorphic rocks are allochthonous and disconnected with folding and thrusting in the foreland or parautochthons and connected with foreland deformation in space and time.

3. GEOLOGIC SETTING AND SAMPLE DESCRIPTION

3.1 Structures and Stratigraphy

The Northern Range of Trinidad is bounded by the Arima Fault to the south and the Northern Coast and Sub-Tobago Terrane faults offshore to the north (Fig. 1b) (Robertson and Burke, 1989; Weber et al. 2015, 2020). The Arima Fault was originally mapped by Kugler (1961) and corresponds to observable meso-scale faults and cataclastic zones (Weber, Ferrill et al., 2001). Previously hypothesized to be an eastward extension of the El Pilar transform fault, the Arima Fault is actually a south-side-down, inactive normal fault that accommodated N–S extension (Weber, Ferrill et al., 2001). The subsurface Caroni fault may instead represent the eastern El Pilar extension (Pindell & Kennan, 2007), though active strike-slip motion now occurs along the Central Range Fault to the south (Fig. 1b; Weber, Dixon, et al., 2001). The North Coast and Sub-Tobago Terrane fault zones (Fig. 1b) accommodate active strike-slip and normal dip-slip between the Northern Range and Tobago terrane (Robertson & Burke, 1989; Weber et al. 2015, 2020). This offshore fault zone also contains *en echelon* normal faults that strike northwest and have moderate to steep northeastern dips (Robertson & Burke, 1989). These *en echelon* structures mirror the late normal faults mapped and observed in the Northern Range at the meso- and macro-scales (Fig. 2) and are attributed by Robertson & Burke (1989) to be related to broad, plate-scale, transform shear. Such structures are also mapped in eastern Paria (Cruz et al., 2007).

At Chupara Point, both Kugler (1961) and De Verteuil et al. (2005) infer the presence of the Chupara Fault, a northwest-striking, steeply dipping, west-side-up normal fault. The inferred Chupara Fault trends NNW-SSE from Chupara Point on the north coast, across the range, potentially extending across the entire range southward to where it is truncated by the Arima Fault near the town of Maturita (Fig. 2; Kugler, 1961; De Verteuil et al., 2005). On the other hand, Potter (1968) inferred a series of short, disconnected, NW-striking fault segments at Chupara Point, Verdant Vale, and along the southern foot of the range. Kugler (1961) mapped the Chupara Fault as one in a series of southeast- and southwest-striking normal faults. Some of the other geologic maps of the range do not show the Chupara Fault (e.g., Saunders et al., 1997). Mapping the Northern Range has been a significant challenge. Kugler's (1961) biostratigraphic approach that proved so successful in Trinidad's sedimentary rocks further south, together with related attempts to establish a protolith stratigraphy in these metamorphic rocks, has largely failed (see below).

The metasedimentary rocks of the Northern Range include predominantly slates, quartz and mica schists, quartzites, and metacarbonates. Mesozoic fossils have been reported from only about a dozen localities scattered in the range (e.g., Dighton-Thomas, 1935; Imlay, 1954; Kugler, 1961; Saunders, 1972; Spath, 1939; Trechmann, 1935); these ages range from Tithonian (Jurassic) (?) to Maastrichtian (Upper Cretaceous) (Fig. 2). Significantly, relict fossils have only been found in the low-grade rocks east of the inferred Chupara Fault and in the fault-bounded, low-grade Laventille metalimestone and Lopinot phyllite along the range front. Apparently, no relict fossils have survived in the higher-grade metamorphism west of the Chupara Fault, which have been isoclinally folded, structurally transposed (i.e., original bedding has been rotated into, cut by, and highly stretched in the S1 foliation), and highly recrystallized. In addition to the relict fossils, two radiometric ages that are highly disparate have been reported from the San Souci metabasalt, which is a small and significant, but poorly studied, poorly mapped, and poorly understood meta-igneous unit in the range (Fig. 2). Wadge & Macdonald (1985) report a whole rock K-Ar protolith age of 87 ± 4.4 Ma, whereas Neill et al. (2014) dismiss the earlier age as erroneous due to alteration and report a 135 ± 7.3 Ma zircon U-Pb crystallization age.

Traditionally it has been assumed, though not demonstrated, that a simple protolith stratigraphy still exists in these metamorphic formations, despite the limitations discussed above, and the fact that they are indeed metamorphic rocks, not sedimentary rocks (Algar & Pindell, 1993; Barr, 1965; Kugler, 1961; Potter, 1973; Saunders, 1997). Even in the western Northern Range, where relict fossils are completely absent, this imagined protolith stratigraphy leads to the erroneous, widespread, and still recently circulating interpretation that the megastructure of the Northern Range is a northward-vergent, overturned, macroscopic anticline (Kugler, 1961; Potter, 1973; Algar and Pindell, 1993; Babb & Mann, 1999). Instead, the sheet dip of the bedding-parallel S_1 foliation is consistently toward the south there and forms a homocline in which the resistant metamorphic units (quartz schists and quartzites) form a series of south-dipping dip-slopes and hogbacks. The De Verteuil et al. (2005) map is the first attempt to abandon the hypothesized protolith stratigraphy and simply map metamorphic rock types as directly observed in the field. We follow a similar approach below as we describe and treat the units in the Northern Range as low-grade metamorphic terranes.

3.2 Petrography and Sample Descriptions

Northern Range protoliths were likely derived from passive margin sediments deposited along the northern edge of South America during and after the breakup of Pangea in the Jurassic and throughout the Cretaceous (Speed, 1985; Frey et al., 1988; Robertson & Burke, 1989; Bartlett et al., 2021). These protoliths were likely carbonates, mudstones, and sandstones, which have been metamorphosed at sub-greenschist to greenschist facies conditions (Frey et al., 1988). The protoliths represent a mixture of continental shelf sedimentary rocks that were deformed and exhumed during and after Miocene collision (Pindell & Kennan, 2001, 2007). The twenty-six samples we collected and analyzed are representative of the six major lithologies from across the Northern Range (Fig. 2) (1) high-grade, foliated marble, (2) low-grade metacarbonate, (3) mica schist, (4) mica-rich phyllite, (5) metasandstone, and (6) carbon-rich slate (Fig. 2 & 3).

The high-grade marbles (Fig. 3a) are all strongly foliated, exhibiting dark bands rich in CM and lighter, carbonate-rich bands. Many of these samples also contain minor sulfides, mainly pyrite and arsenopyrite; some of the pyrite grains have been weathered and broken down into iron oxides. The low-grade metacarbonates (Fig. 3b; metacarbonate in Fig. 2) generally preserve primary sedimentary structures and textures (Fig. 3c). Fossil shells and ooids are common in many of these rocks, which exhibit low-strain, ductile deformation at the micro-scale (Fig. 3c). Some low-grade metacarbonates are crosscut by calcite-filled veins indicative of brittle extensional deformation and precipitation from metamorphic fluids. Further, later stage brittle deformation is recorded by the cross-cutting of calcite veins by fractures.

The quartz-mica schists (Fig. 3d) mainly crop out in the western Northern Range. These schists are well-foliated and consist of a greenschist-facies mineral assemblage (muscovite + chlorite + quartz + plagioclase + CM ± biotite ± oxides or sulfides). These rocks are variable in both composition and structure, showing a wide range of mica content (5–25%). Coarser-grained rocks tend to have less mica and a less evident foliation. These are the only rocks seen to host metamorphic biotite in substantial quantities, indicating they are likely of the highest grade in the study area. Quartz and calcite grains in these rocks are thermally recrystallized, as indicated by the presence of undulose extinction in quartz and the presence of triple-point grain boundaries (Fig. 3d). Recrystallization likely occurred during deformation, as evidenced by the oriented stretching elongation of quartz parallel to the S_1 foliation plane (Fig. 3d). This elongation is consistent with the observations of Weber, Ferrill, et al. (2001), who attributed the foliation to the first stage, D_1, of Northern Range deformation. At the microscopic scale, CM is observed to be concentrated in mica-rich bands related to the tight F_1 folds that transpose bedding (S_0) into S_1 and later kink bands.

The phyllites (Fig. 3e) are extremely rich in sericite, and are fine-grained, and well foliated. The phyllitic foliation is defined by sericite ± chlorite, with some degree of post-S_1 crenulation common in these rocks. The multiple foliation planes recorded in these phyllites reflect the first two phases of Northern Range deformation, which predominantly occurred in the ductile regime (Weber, Ferrill, et al., 2001). The CM content of the phyllites is variable; only a few samples had sufficient CM for RSCM analysis. Carbonaceous material with radial growth textures 0.1–0.3 mm in length is also observed in some of these rocks and it appears to be post-kinematic as it crosscuts foliation (Fig. 3f); multiple explanations are possible for their formation (cf. Luque et al., 1998; Rumble, 2014). Their composition was confirmed to be carbonaceous through electron probe microanalysis (EPMA).

Metasandstones are composed mainly of subangular quartz grains (Fig. 3g), but also contain minor mica and calcite along with CM. The weakly-metamorphosed rocks of this type come from the eastern and central Northern Range and are typically non-foliated to weakly foliated. Atypically strong foliation and folding were observed in sample NR-1 (Fig. 3h). Sample NR-1 (equivalent to NR-3) displays isoclinal microfolds, likely representing parasitic folds created during early semi-ductile deformation. Metasandstones from the central Northern Range display a weak foliation, but some quartz grains experienced modest shape changes, likely through a combination of pressure solution and low-temperature crystal plasticity (Weber, Ferrill, et al., 2001). Minor chlorite is seen in central Northern Range samples. However, it is generally absent in the eastern metasandstones, reflecting either a variation in composition or metamorphic grade; limited evidence suggests the former (Frey et al., 1988).

The dark, carbon-rich slates (Fig. 3i) are compositionally and texturally similar to the phyllites, but tend to have a lower mica content and higher content of carbonate minerals (Fig. 4a) and CM. These rocks are very fine-grained and well foliated, containing minor amounts of quartz, plagioclase, and sulfides that mainly occur as framboidal pyrite. These rocks have a well-developed, early S_1 slaty cleavage that is weakly crenulated by subsequent deformation.

4. METHODS

4.1 Electron Probe Microanalysis

Quantitative wavelength-dispersive spectrometry and backscattered electron (BSE) imaging were carried out using a JEOL JXA-8230 electron probe microanalyzer (EPMA) at the University of Toronto. Quantitative analyses employed a 10 nA beam current, 15 kV accelerating voltage, and off-peak background corrections. The electron beam was defocused (10 µm) to minimize beam damage on carbonate minerals.

4.2 RSCM Geothermometry

Thin sections were polished to a thickness of ~35 μm and made in accordance with the specifications of Beyssac et al. (2003) for RSCM analysis. Rocks were cut perpendicular to bedding or foliation planes and parallel to lineation in order to reduce within-sample heterogeneity caused by the anisotropy of CM (Beyssac et al., 2003). The carbonaceous inclusions in transparent minerals were analyzed using two Raman spectrometers: 15 samples were analyzed at the Department of Earth Sciences at the University of Turin (UNITO) in Turin, Italy, and another 18 samples were analyzed at the Royal Ontario Museum (ROM) in Toronto, Canada. Seven samples were analyzed on both spectrometers to ensure inter-instrument consistency. Only one sample (DT-93-1) was omitted due to a lack of CM.

Raman spectra were collected using a LabRAM HRVIS from Horiba Jobin Yvon Instruments at UNITO and a Horiba LabRAM ARAMIS micro-Raman spectrometer at the ROM. Both spectrometers were calibrated with a silicon standard and used a 532 nm solid-state neodymium laser. The lasers were dispersed using 1200 gr/mm gratings and focused on the samples using 100x objectives with a numerical aperture of 0.9. In order to avoid laser-induced heating, a low laser power (<5 mW) was used during analysis (Beyssac et al., 2003). At UNITO, no filter was required; at the ROM, the D1 or D0.6 filters (10% and 25% transparency respectively) were used to ensure a laser power below 5 mW.

A combination of transmitted and reflected light was used to target CM located below the surface of the host minerals to avoid artificial defects induced by sample preparation (Beyssac & Lazzeri, 2012; Beyssac et al., 2003). At least 15 spectra were collected for each sample. The spectral baselines were corrected, and the spectra were fitted using the Peakfit software (AISN Software Inc., 1995). Wherever possible, a linear baseline was used for the correction, but micaceous samples sometimes required a best-fit baseline correction as the fluorescence of mica is detectible within the range of 700–2000 cm^{-1} (Beyssac & Lazzeri, 2012).

For samples showing CM Raman spectra characteristic of high-temperature conditions (>330 °C; e.g., SC-2b, Fig. 5a), we apply the 532 nm laser-based calibration of Aoya et al. (2010) (Eq. 1) along with the 514 nm laser-based calibration of Beyssac et al. (2002) (Eq. 2) as a reference. These spectra were fitted with three bands and Voigt peaks, which converged to a unique solution (Beyssac & Lazzeri, 2012; Lahfid et al., 2010). For samples showing CM Raman spectra characteristic of low-temperature conditions (<350 °C; e.g., T94-3, Fig. 5b), we apply the 514 nm laser-based calibration of Lahfid et al. (2010) (Eq. 3) and the two 532 nm laser-based calibrations of Kouketsu et al. (2014) (Eq. 4 & 5). For the Lahfid et al. (2010) calibration, these spectra are decomposed into five bands; the use of Lorentzian profiles was necessary to reduce the degree of freedom and allow a unique solution to be obtained (Beyssac & Lazzeri, 2012; Lahfid et al., 2010). The samples were then refit following Kouketsu et al. (2014) to use their calibrations (see below). The temperatures were then calculated using the area ratios of the peaks based on the respective thermometer calibrations (see Aoya et al., 2010; Beyssac et al., 2002; Lahfid et al., 2010).

Most samples displayed solely high- or low-temperature spectra, whereas nine samples of intermediate temperature (300–360 °C) feature a mixture of 3- and 5-band spectra. In the case of the nine samples with both types of spectra, the Aoya et al. (2010) calibration was applied to 3-band spectra and the Lahfid et al. (2010) calibration was applied to 5-band spectra. We note that only four reported temperatures are the averages of both calibrations that statistically overlap. The second calibration applied to the other five samples is rejected as outliers (Table 1). For example, among the fifteen datapoints of 93-T-CB, three 5-band spectra yield much lower temperatures (284 ± 10 °C) than the twelve 3-band spectra which make up the majority (366 ± 5 °C; Table S1). On the other hand, one datapoint of MAT-1(3) shows a 3-band spectrum that yields a temperature of 472 °C, >100 °C higher than the average of the 5-band spectra (340 ± 4 °C); this CM inclusion, consistent with the temperature calculated using the Beyssac et al. (2002) calibration, is interpreted as detrital CM (Table S1). In both cases, the outliers were omitted when reporting the final temperature.

A second fitting of the data was done on samples with peak temperatures below 400 °C in accordance with the specifications of Kouketsu et al. (2014). These calibrations utilize 3–5 peaks which allow for the calculation of peak temperature based on the full width at half maximum (FWHM) of the D1 and D2 bands (Kouketsu et al., 2014). A second fitting ensured all spectra treated were fit with a linear baseline in the range of 1000–1750 cm^{-1} with pseudo-Voigt (Gaussian-Lorentzian sum) functions in accordance with Kouketsu et al. (2014). Some peaks were fixed based on the characteristics of the Raman spectra, such as the intensity ratio of the main D and G bands, to allow for convergence to a unique solution (Kouketsu et al., 2014).

Following these calibrations, R2 and RA1 represent the area ratios between the main D band and the entire spectrum in high- and low-temperature samples, respectively, with $FWHM_{Dx}$ representing the full width at half maximum of the corresponding defect band (D1 or D2) (Beyssac et al., 2002; Kouketsu et al., 2014; Lahfid et al., 2010).

$$T(°C) = 221.0(R2)^2 - 637.1(R2) + 672.3 \quad (1)$$

$$T(°C) = -445(R2) + 641 \quad (2)$$

$$T(°C) = (RA1 - 0.3758)/0.0008 \quad (3)$$

$$T(°C) = -2.15(FWHM_{D1}) + 478 \quad (4)$$

$$T(°C) = -6.78(FWHM_{D2}) + 535 \quad (5)$$

5. RESULTS

5.1 Carbonate Thermometry

Weber, Ferrill et al. (2001) presented comprehensive documentation and analyses of the calcite microstructures in the Northern Range metasedimentary rocks (see their Figure 8). Depending on the metamorphic grade, the calcite microstructures range from thin calcite twins in rocks with intact and preserved sedimentary textures to plastically deformed, fully recrystallized, mechanical twins. Given that these dynamically recrystallized calcite grains are commonly present in crosscutting veins, the highest temperatures derived from calcite microstructures in that study can thus be considered as a lower bound for peak metamorphic temperatures. Here, we attempt Ca-Mg-Fe thermometry between calcite and dolomite in a slate sample with disseminated calcite and dolomite (NR-5, equivalent to NR-2), and show that this thermometer is not applicable due to a lack of chemical and textural equilibrium.

A BSE image representative of the mineral assemblage and texture of NR-5 is presented in Figure 4a. Ankerite grains (dol in Fig. 4) are larger and more euhedral than calcite. The schistosity bends and forms pressure shadows around ankerite micro-porphyroblasts. The ankerite has a Mg# (=Mg / [Mg + Fe]) ~0.4 and Ca content ~0.54 per 3 O. The calcite contains minor (~0.04 per 3 O) Fe, Mg and Mn (Fig. 4b). The bending of schistosity around both calcite and ankerite grains suggests that both are likely pre-kinematic, potentially pointing to the presence of both minerals during peak metamorphism. However, the two minerals show contrasting crystal habits, with euhedral ankerite exhibiting stability while anhedral calcite grains likely reequilibrated with the surrounding matrix during retrograde metamorphism.

Along with the disequilibrium textures, the analyzed carbonates display a high degree of scattering on the carbonate phase diagrams, yielding a large temperature range (Fig. 4b). While the thermodynamic models (Anovitz & Essene, 1987) include uncertainties and equilibrium assumptions, the variability of measured carbonate concentrations adds to the concern of applying this particular mineral-pair thermometer. Calcite microstructural geothermometry from the adjacent area yields 200–250 °C (Weber, Ferrill, et al., 2001), but inferred phase relations suggest disequilibrium between calcite and dolomite at 250 °C (Fig. 4b). In contrast to the >300 °C temperature recorded by RSCM (see below), the calcite composition and microstructures must have been modified during retrograde metamorphism. In sum, as in Frey et al. (1988), conventional geothermometers could not resolve the field gradient across the low-grade eastern Northern Range due to the violation of several of the required fundamental assumptions.

5.2 RSCM Data and Thermometry

Representative low-temperature and high-temperature Raman spectra are presented in Figure 5 to illustrate the decomposition of Raman spectra for RSCM calculation. A complete set of fitted spectral data are provided in the supplementary material (Tables S1 & S2; Gennaro et al., 2021), and a complete set of results based on spectra fitting are presented in Table 1. In the first-order region (700-2000 cm^{-1}), the low-temperature and high-temperature samples show characteristic RSCM features such as the presence of five (G, D1, D2, D3, D4) and three (G, D1, D2) major Raman bands, respectively (Fig. 5; Beyssac & Lazzeri, 2012; Beyssac et al., 2002; Lahfid et al., 2010). Samples of intermediate temperature (~340–380 °C) were also fitted with four bands in accordance with Kouketsu et al. (2014). Along with the major D and G peaks, spectra from carbonate-rich samples show calcite peaks at ~1100 cm^{-1}, which were minimized as much as possible in measurements. Values of the R^2 fitting correlation coefficient on samples with calcite peaks may be low as this peak is removed after fitting to allow for calculations using only peaks associated with CM.

The centers of fitted G bands show moderate variation (Table S1; Fig. S1) from fully ordered graphite (1582 cm^{-1}; Wang et al., 1990), especially the low-temperature samples analyzed at UNITO (Fig. S1). The downshifted Raman spectra might reflect amorphization by laser heating (Kagi et al., 1994; Iwasaki et al., 2013; Nakamura et al., 2019), as Raman spectra of low-grade CM are ideally obtained with laser powers of <1 mW to avoid laser-induced artifacts (Nakamura et al., 2019). Nonetheless, we note that the apparent temperatures calculated using 3- and 5-band calibrations (Aoya et al., 2010 and Lahfid et al., 2010, respectively) do not show any systematic correlation with the shifts of G bands (Fig. S1). Given that the intrinsic uncertainty of RSCM on low-grade samples is unquantified and potentially considerable, we reasonably regard the temperatures as robust results.

The temperatures from the two Kouketsu et al. (2014) calibrations display up to 100 °C variations between the temperatures calculated using the two calibrations on the same sample (Fig. 6 inset). The FWHM of G and D bands has been known to vary as a result of laser-induced heating at laser powers above 1 mW, thus laser-induced heating is the likely cause of this discrepancy (Iwasaki et al., 2013, Nakamura et al., 2019). This is especially evident if the downshift of the G band is used as a proxy for laser-induced heating. Samples with higher scatter in the position of the G band tend to show greater disagreement between the D1- and D2-based calibrations of Kouketsu et al. (2014) (Fig. S1). Therefore, while laser-induced heating does not significantly affect the temperatures of the Aoya et al. (2010) or Lahfid et al. (2010) calibrations in our analysis, the temperatures derived from the Kouketsu et al. (2014) thermometer are considered to be significantly altered and are not used for interpretation.

Our new RSCM temperatures range from 310 ± 13 °C to 465 ± 30 °C (Lahfid et al. 2010 and Aoya et al. 2010 calibrations; 1σ), with an outlier at 497 ± 27 °C (sample M-4). Figure 5c shows the evolution of the acquired spectra with increasing metamorphic temperature. The spectral evolution shows an increase in the intensity ratio of the main D and G bands (I_D/I_G) until about 350 °C, where the main G peak then begins increasing in intensity and area as the D peak decreases. In low-temperature spectra, the D3 and D4 bands decrease in area as temperature increases, and they disappear at around 350 °C. Above this threshold, the D1 and D2 bands decrease in area relative to the G composite band, suggesting progressive graphitization (Beyssac et al., 2003).

We also assess the inter-instrument correlation between the spectra collected at UNITO and the ROM, plotting the calculated temperatures from both spectrometers against a 1:1 line (Fig. 6). The reproducibility of the high-temperature spectra is very good. However, the lower temperature spectra display a larger inter-instrument error regardless of the calibration used. A degree of inter-instrument error is to be expected, has been observed in the past, and is caused by differences in analytical settings such as laser power, the instrument's CCD, and slit spacing on the diffraction grating (Lünsdorf et al., 2013). The increased inter-instrument error in the low-temperature region may be due to differences in laser power, despite being kept below 5 mW, as laser-induced heating may still induce defects in the Raman spectrum at this energy, especially in highly amorphous CM (Beyssac et al., 2003, Kagi et al., 1994; Iwasaki et al., 2013; Nakamura et al., 2019). With regards to the scatter of low-temperature data, the calibrations for low-temperature spectra are more complex as graphitization below 330 °C is affected by variables other than just temperature (Lahfid et al., 2010). Furthermore, the RSCM calibrations, especially at low temperatures, are highly sensitive to the fitting and baseline correction method used (Beyssac & Lazzeri, 2012; Lünsdorf et al., 2013). For consistency, and to reduce the variability caused by inter-instrument error and laser-induced heating, samples from the ROM were used in all cases where samples were analyzed using both spectrometers.

The spatial variation of temperatures exhibits an increase from east to west across the Northern Range (Fig. 7a), in agreement with previous studies (Frey et al., 1988; Weber, Ferrill, et al., 2001). The Lahfid et al. (2010) RSCM results yield temperatures around 320 °C in the easternmost parts of the Northern Range, which increase westward to about 360 °C in the central Northern Range (Fig. 7b). Temperatures of ~360 °C in the central Northern Range are predicted by both low-temperature calibrations. An abrupt temperature difference is seen in the central Northern Range across the previously mapped Chupara Fault (De Verteuil et al. 2005; Kugler, 1961). To the west of this fault, RSCM records peak temperatures of around 450 °C, except for the two samples at ~420 °C in the vicinity of the fault. The temperature difference between the eastern (337 ± 10 °C; Lahfid et al. (2010) calibration) and western segments (442 ± 16 °C; Aoya et al. (2010) calibration), within ~5 km, is 105 ± 19 °C, and a two-tailed Student's t-test indicates that the means are statistically different at the 99% confidence level. Qualitative observation of the Raman spectra corroborates the significant temperature difference between the eastern and western samples. The presence of significantly different Aoya temperatures in the east and west further corroborates this difference as these were derived using the same calibration and represent a degree of internal consistency. The temperatures are internally consistent within the western block, with the eastern block showing higher variation, particularly in the easternmost regions of the Northern Range. Samples in the east gradually increase in temperature from east to west, though they remain close to 340 °C. In addition, samples in the southwestern Northern Range are bounded by the Arima Fault and perhaps additional bounding faults, and typically show lower temperatures (350–410 °C) than their northwestern counterparts (~450 °C; Fig. 7a).

6. Discussion

6.1 Metamorphic Field Gradient and Faulting

Our RSCM data not only corroborate the existence of a geothermal gradient across the Northern Range, but now resolve that this gradient is discrete. The thermal discontinuity in the central Northern Range (Fig. 7a, b) juxtaposes high- (442 ± 16 °C) and low-temperature (337 ± 10 °C) blocks at Chupara Point. Given the abrupt temperature change we observe, a structural discontinuity must exist to accommodate it. The most probable candidate for such an intra-range boundary is the Chupara Fault as mapped by Kugler (1961) and De Verteuil et al. (2005). The Chupara Fault is one in a series of SE-striking normal faults that were hypothesized by Algar & Pindell (1993) to represent the final, transtensional stage of Northern Range deformation and presumed to be related to a change in the direction of Caribbean-South American plate motion from collisional to right-lateral strike-slip (transform).

Much of our RSCM data comes from the north coast, leaving the southern mountain front and internal segment of the metamorphic discontinuity more poorly constrained. Here, we refine slightly the Chupara Fault trace as mapped by De Verteuil et al. (2005), which was based on differences in metamorphic rock types and inferred differences in grade using microstructures. Topographic radar images show possible minor differences across the northern trace of the Chupara Fault; these diminish to the south (Fig. 7a), suggesting that the Chupara Fault is likely inactive. Future sampling in the range interior and more RSCM data can help to better define the position of the southern extent of the thermal gradient we observe as well as that of the Chupara Fault. We also note that we lack the data needed to speculate whether or how the onshore Chupara Fault relates to any offshore faults (e.g., Robertson and Burke, 1989).

In the southwestern Northern Range, the lower temperature samples of 350–410 °C in the Chancellor schist are separated from the main western block by a fault previously mapped by De Verteuil et al. (2005) (Fig. 7a). This fault may accommodate up to 4 km of vertical slip based on a typical passive margin geotherm of 25 °C/km (Weber, Ferrill, et al., 2001). The temperature difference between the northwesternmost rocks and the Chancellor schist in the southwest mirrors the S–N grade increase observed in Paria, eastern Venezuela by Cruz et al. (2007, and references therein). Two samples ~3–5 km west of the Chupara Fault display slightly lower peak temperatures (~420 °C) than others surrounding them and thus may be separated from the rest of the western block by an additional splay fault(s) (e.g., Fig. 3b in Algar & Pindell, 1993) or some other unrecognized fault(s) (Fig. 2; De Verteuil et al., 2005). Finally, one outlier in the west, sample M-4, displays scattered, high peak temperatures of 497 ± 27. This sample was collected from a shear zone where processes such as frictional heating during faulting may have altered the CM structure, leading to an increased RSCM-derived temperature (Furuichi et al., 2015).

The RSCM results from within the eastern block display an additional, less pronounced, systematic scatter (Fig. 7b), which might reflect second-order gradients or discontinuities that are difficult to quantify. This can be seen qualitatively by comparing the CM Raman spectra of samples from the eastern and central Northern Range (following, e.g., Kouketsu et al., 2014). We also note that the increased elongation of quartz grains in central metasandstones indicates a higher degree of quartz ductility and therefore, a potential for deeper burial and higher-grade metamorphism than rocks further east (Weber, Ferrill et al., 2001). Furthermore, the Sans Souci metabasalt (Fig. 2) along the northeast coast has a prehnite-pumpellyite mineral assemblage, while the rest of the eastern and central Northern Range appears to be mineralogically closer to or within the higher-grade greenschist facies (Frey et al., 1988). The RSCM data in the eastern block are sparse, so we are unable to rule out faulting as a cause of the potential eastern thermal gradient, and therefore further work is needed to confirm and more fully quantify the nature of this gradient.

6.2 Timing of Metamorphism and Fault-related Exhumation

We next used metamorphic ages and low-temperature thermochronology data, together with our RSCM results, to infer the timing of fault slip, differential bedrock cooling, and inferred exhumation along the block-bounding Chupara Fault. Our RSCM data provide new constraints and support for the previously proposed Miocene age of the Northern Range. $^{40}Ar/^{39}Ar$ spectra from the Northern Range, introduced in abstract form (Foland et al., 1992) and in a field guide (Weber & Arkle, 2015) all indicate ages of ca. 25–30 Ma (Fig. 8b). In addition, Speed et al. (1997) determined the $^{40}Ar/^{39}Ar$ age of well-ordered (10Å), syn-metamorphic white mica of the Dragon Gneiss in Paria, Venezuela, presenting an age of 23.3 ± 0.2 Ma (between 8% and 95% Ar release). A second age in that study yielded a total gas age of 34.3 Ma with a plateau around 21 Ma (Speed et al., 1997). We note that the temperature estimates in other geothermometry studies (<400 °C; Frey et al., 1988; Weber, Ferrill, et al., 2001) are all lower than, or close to, the closure temperature of the muscovite $^{40}Ar/^{39}Ar$ system (380 ± 30 °C; Harrison et al., 2009). Because the $^{40}Ar/^{39}Ar$ ages are mainly taken from metamorphic micas, previous studies regard them as representative of the timing of peak metamorphism. However, some of the younger ages (21-23 Ma) might have experienced Ar loss or resetting during cooling.

Zircon fission track (ZFT) data from the Northern Range show a general pattern with reset ages of ~12 Ma in the west (Fig. 8b), whereas most eastern zircons are un-reset and display ages ranging from ~80–200 Ma (Algar et al., 1998; Arkle et al., 2021; Weber, Ferrill, et al., 2001). Our new RSCM temperatures from both the east and west (310–450 °C) all exceed the ZFT closure temperature of 240 ± 30 °C (Brandon et al., 1998). This produces some discrepancy because of the presence of detrital ZFT ages at these temperatures; this relationship is also seen in studies of Taiwan's mountain ranges (Beyssac et al., 2007; Simoes et al., 2007). These discrepancies are thought to result from the complexities of zircon annealing, including effects related to variable thermal histories and a range of physical and chemical properties of zircon grains (Brandon et al., 1998).

Post-metamorphic thermochronology data from the Northern Range indicate significant differential exhumation of the eastern and western blocks between ~10–4.5 Ma (Arkle et al., 2021), which we suggest corresponds to the period of most active slip of the Chupara Fault (Fig. 8). Arkle et al. (2021) document rapid bedrock cooling and exhumation (~1.5 mm/yr) of the western Northern Range, wherein >7 km of rock was exhumed from ~10–4.5 Ma (Fig. 8b). During the same time period, thermal models indicate that pre-Pliocene exhumation of the eastern Northern Range was only <2 km (Fig. 8a). Although exhumation was clearly focused within the western and eastern crustal blocks of the Northern Range, mechanisms of differential exhumation such as discrete faults or other structures that dissect the mountain range could not previously be identified. We propose that the east-to-west offset of RSCM temperatures we observe need to be consistent with the magnitude and style of offset on the Chupara Fault. The 4 Ma–Recent differential exhumation between the eastern and western Northern Range could be accommodated by faulting, such as reactivation of the Chupara Fault. However, no geomorphic or geodetic evidence supports its Quaternary to Recent slip.

In the discussions above, we assume that cooling was mainly induced by exhumation. Evidence at the regional scale suggests that a majority of the differential cooling in the Northern Range can most reasonably be attributed to exhumation driven by normal faulting and erosion. Bedrock exhumation by erosion off the top of the North Range is supported by the initiation of high sedimentation rates in the Gulf of Paria basin starting at ~4 Ma and in the North Coast basin at ~12 Ma (Flinch et al., 1999). The late-stage normal faults pervasive throughout and surrounding the Northern Range (Algar & Pindell, 1993; Kugler, 1961; Weber et al., 2015) also indicate favorability for fault-driven exhumation following peak burial. Furthermore, the timing of increased sedimentation, e.g., as described by Flinch et al. (1999), matches the timing of accelerated cooling in the west (late Miocene–Pliocene), suggesting a coupling between sedimentation and bedrock cooling due to erosional exhumation of the Northern

Range. On the other hand, Pindell and Kennan (2007) suggest that the underplating of cold proto-Caribbean material beneath the western Northern Range is responsible for its cooling (also see 6.3). However, this sort of regional-scale thermal conduction would presumably produce a more gradual temperature profile than that seen in our new RSCM data. In addition, such underthrusting is postulated to have occurred before the ~12 Ma Caribbean-South American collision in Trinidad (Algar & Pindell, 1993; Pindell & Kennan, 2007). If underthrusting did cause significant cooling, its effect should therefore have been strongest before 12 Ma, precluding it from contributing significantly to the younger thermal gradient that we observe. Advection of cold fluid can, in principle, also produce steep field gradients (e.g., Rogiers et al., 2014), though its durations are shorter (< 0.1 Myr) and depths are typically much shallower (< 2 km) than the *t-T* histories documented herein.

6.3 Mechanisms of Hinterland Metamorphism

Most models attribute metamorphism and subsequent exhumation of the Northern Range, as well as of Venezuela's Cordillera de la Costa, to the oblique collision between the Caribbean and South American Plates (Algar & Pindell, 1993; Garciacaro et al., 2011; Pindell & Kennan, 2001; Robertson & Burke, 1989). It is also generally agreed upon that exhumation occurred in Trinidad in the mid-Miocene, although its mechanism is disputed (Algar & Pindell, 1993; Arkle et al., 2017; 2021; Clark et al., 2008; Cruz et al., 2007; Speed, 1985; Weber, Ferrill, et al., 2001). Our new RSCM temperature estimates exceed temperature estimates from all previous metamorphic studies in the Northern Range (300–350 °C, Frey et al., 1988; 250–400 °C, Weber, Ferrill, et al., 2001). If attributed to depth, the higher metamorphic grades call for revision of tectonic models to accommodate deep burial; here, we suggest that the required deep burial likely occurred through 1) the incorporation of additional shelf sediments into the fold-thrust or accretionary wedge (e.g., Pindell & Kennan, 2001), and 2) transpression acting to squeeze this material between the two plates, allowing for both increased crustal thickness and orogenic uplift (e.g., Cruz et al., 2007).

The Northern Range rocks likely began as a mixture of passive margin (metamorphosed mudstone and turbidites) and continental shelf (becoming marbles and metasandstones) sedimentary protoliths (Fig. 9a). The sequence was incorporated into a fold-thrust wedge along the leading edge of the Caribbean plate with varying degrees of transport having been inferred (Fig. 9b; Pindell and Kennan, 2001, 2007; Speed, 1985). The two end-members contrasting oblique collision models depict the entire south Caribbean metamorphic hinterland, including the Northern Range, either as an allochthon (Audemard, 2009; Avé Lallemant, 1997; Pindell & Kennan, 2001) or a parautochthon (Cruz et al., 2007; Russo & Speed, 1992, 1994).

Tomographic imaging beneath northern South America reveals a sinking mass, which has been associated with either a southward-subducting proto-Caribbean plate (Pindell and Kennan, 2001, 2007) or the removal of South American lithosphere along a near vertical crustal STEP (Levandar et al., 2014). The allocthonous model attributes deformation to events occurring since the early Paleocene due to the subduction of a proto-Caribbean plate beneath South America. Pindell and Kennan (2007) suggest that the Northern Range represents the accretion of both proto-Caribbean and Caribbean trench sediments. However, no magmatism associated with the southward subduction of a proto-Caribbean lithosphere beneath South America has been found on the South American continent. The lack of upper-plate volcanism and differing seismic tomographic interpretations leave the existence of a subducted proto-Caribbean plate open to debate (Levander et al., 2014; Pindell & Kennan, 2001, 2007). In addition, the accretionary model (Pindell & Kennan, 2001, 2007) requires about 200 km of displacement since 10 Ma to bring the Northern Range to its current position. This value contrasts with <100 km of displacement along the El Pilar and associated transform plate boundary faults (Audemard, 2009, and references therein). We also note that the 450 °C temperature from our new RSCM results suggests deeper burial than is typical for both sedimentary and structural burial within accretionary wedges. In addition, the lack of high-pressure minerals like sodic-calcic amphiboles and garnet rules out potential high-P/T metamorphism of an oceanic slab such would be expected from the subduction of a large, mature "proto-Caribbean" plate. Thus, we prefer a model with significant crustal shortening associated with tectonic burial and crustal downflow to bring the Northern Range protoliths down to depths of ~17 km (25 °C/ km geotherm; c.f. Cruz et al., 2007), although we cannot rule out the possibility of some pre-collisional influence from a proto-Caribbean plate.

Cruz et al. (2007) suggest that the Venezuelan metamorphic belt was exhumed as a two-sided wedge, such as those described in the numerical models of Willet et al. (1993); as the Northern Range represents an extension of this belt, the same mechanism may apply. The geometry of a two-sided wedge (e.g., Cruz et al. 2007) could have been induced in Trinidad by northward subduction of the pre-collisional oceanic portion of the South American plate beneath the Caribbean plate. The model is supported by the oblique-normal shear indicators and SW-plunging lineations observed in the Cordillera de la Costa, Venezuela (Cruz et al., 2007). In a two-sided wedge, the material is accreted in the foreland and moves towards the retro-wedge of the hinterland, and thus, the metamorphic grade increases towards the retro-wedge (Willett et al., 1993). Topographically, a two-sided wedge presents a low-angle taper on the "pro-wedge" portion on the side of the subducting slab, while the "retro-wedge" is on the side of the overriding plate and displays a high-angle taper (Willet et al., 1993). The RSCM data from the southwestern Northern Range are consistent with this model, which predicts a metamorphic temperature increase towards the retro-wedge. The Chancellor schist displays lower RSCM temperatures than those in the rest of the western block (340–410 °C, purple unit in Fig. 7a). The range-front position of the Chancellor schist, and the fault-bounded, low-grade Laventille metalimestone and Lopinot phyllite (Fig. 2), which display a range-front fold geometry of upright NE-SW trending folds, could reflect the modified southern side of a bivergent wedge (e.g., De Verteuil et al., 2005; Teyssier et al., 2002; Weber, Ferrill, et al. 2001). Farther south in the Central Range, which represents a major foreland fold-thrust structural culmination, <4 km of exhumation occurred from 18–11 Ma (Giorgis et al., 2017). Crustal shortening, development of a deep crustal root, and the deformation of the South American margin (Cruz et al., 2007), likely produced the observed metamorphic grades and significant burial depths of the Northern Range rocks (Fig. 9b). In sum, the lithological, structural, and thermal data of the Northern Range are all consistent with a two-sided wedge model and collision mechanism.

The bedrock cooling models of Arkle et al. (2021) indicate that a significant amount of post-collisional cooling and exhumation occurred in the western Northern Range from ~10–4.5 Ma, while little cooling and exhumation occurred in the east during that same time period. Arkle et al. (2021) further speculate that the STEP edge passed eastward under Trinidad following oblique collision (Fig. 9c), creating a series of late-stage, en echelon normal faults that accommodated the overall strike-slip (transform) motion that is also pervasive throughout the Northern Rin Trinidad (Algar & Pindell, 1993; De Verteuil et al., 2005) and eastern Venezuela (Cruz et al., 2007). We propose that the Chupara Fault may be such a post-orogenic, extensional feature (Figs. 2, 7a, 9c). Thus, the activity of the Chupara Fault may be linked to the exhumation of the deeply buried rock in the western Northern Range that we document using RSCM data, perhaps as the STEP front migrated eastward (Fig. 9c). Thermal models, erosion data, and other regional geomorphic data also indicate that differential cooling and exhumation inverted around 4.5 Ma (Arkle et al., 2017: 2021). The STEP edge at this time (~4.5 Ma) would have moved sufficiently far to the east, became insignificant in the Northern Range, and brought the activity along the Chupara Fault to an end (Fig. 9d).

7. CONCLUSIONS

RSCM geothermometry provides important constraints on the peak metamorphic temperatures of key lithologic units across the Northern Range and helps to fill vital gaps in our understanding of its thermal history. The RSCM data collected across a broad swath of the range reveals a discrete thermal gradient with peak metamorphic temperatures of 337 ± 10 °C in the east and 442 ± 16 °C in the west, confirming the field gradient proposed by Frey et al. (1988) and demonstrated by Weber, Ferrill, et al. (2001). The abrupt temperature discontinuity of 105 ± 19°C located at Chupara Point corresponds to the location of the previously mapped Chupara Fault. Further field work is required to better constrain the precise location, timing, and kinematics of the Chupara Fault. Our new RSCM temperature estimates surpass all previous estimates and thus require greater burial depths of Northern Range rock. We speculate that Miocene oblique plate motion created a two-sided wedge in which parautochthonous Northern Range rocks were incorporated into a fold-thrust hinterland wedge. Our new peak temperatures, together with thermochronological data, lead us to interpret that the Chupara Fault is likely the main structure that accommodated differential exhumation between the eastern and western Northern Range. The distinctly different cooling trajectories suggest that the Chupara Fault was likely active from ~10–4.5 Ma, though activity before or after this time period cannot be completely ruled out.

Acknowledgments

This study was inspired by a departmental field trip to the Caribbean, organized and led by Professor Emeritus Edward Spooner and Laurent de Verteuil, along with undergraduate students Colin Roth and Jason Hinde. The Raman analyses and training at the University of Turin were supported by an Undergraduate Student Research Award of the Natural Sciences and Engineering Research Council (NSERC USRA, reference number 501984) to I.G. and a MIUR grant Levi Montalcini to A.V.B. The study is also supported by NSERC (Discovery Grant RGPIN-2018-03925 to X.C.). This work is part of a project that has received funding from the European Research Council (ERC) under the European

Union's Horizon 2020 research and innovation programme (Grant agreement No. 864045). We thank Veronica DiCecco and Yanan Liu for help with Raman spectroscopy and the electron microprobe analysis, at the Royal Ontario Museum and the University of Toronto respectively. Sample collection by Adam Brudner is gratefully acknowledged.

References

Algar, S. T., & Pindell, J. L. (1993). Structure and deformation history of the Northern Range of Trinidad and adjacent areas. *Tectonics*, 12(4), 814–829. https://doi.org/10.1029/93TC00673

Algar., S. T., Heady, E. C., & Pindell, J. L. (1998). Fission-track dating in Trinidad: Implications for provenance, depositional timing and tectonic uplift. In Pindell, J. L., & Drake, C. (Eds.), *Paleogeographic evolution and non-glacial eustasy, northern South America* (Special Publication 58, pp. 111–128). Tulsa, OK: Society of Economic Paleontologists and Mineralogists.

Anovitz, L. M., & Essene, E. J. (1987). Phase Equilibria in the System CaCO3-MgCO3-FeCO3. *Petrology*, 28(2), 389–414. https://doi.org/10.2473/shigentosozai1953.98.1131_441

Aoya, M., Kouketsu, Y., Endo, S., Shimizu, H., Mizukami, T., Nakamura, D., & Wallis, S. (2010). Extending the applicability of the Raman carbonaceous-material geothermometer using data from contact metamorphic rocks. *Journal of Metamorphic Geology*, 28, 895–914. https://doi.org/10.1111/j.1525-1314.2010.00896.x

Arkle, J. C., Owen, L. A., Weber, J. C., Caffee, M. W., & Hammer, S. (2017). Transient Quaternary erosion and tectonic inversion of the Northern Range, Trinidad. *Geomorphology*, 295, 337–353. https://doi.org/10.1016/j.geomorph.2017.07.013

Arkle, J. C., Weber, J. C., Enkleman, E., Owen, L. A., Govers, R., Denison, C., et al. (2021). Exhumation of the coastal metamorphic belt above a subduction-to-transform transition, in the southeast Caribbean plate corner. *Tectonics*, 40(8). https://doi.org/10.1029/2020TC006414

Audemard, F. A. (2009). Key issues on the post-Mesozoic Southern Caribbean Plate boundary. *Geological Society Special Publication*, 328, 569–586. https://doi.org/10.1144/SP328.23

Avé Lallemant, H. G. (1997). Transpression, displacement partitioning, and exhumation in the eaastern Caribbean / South American plate boundary zone. *Tectonics*, 16(2), 272–289. http://dx.doi.org/10.1029/96TC03725

Babb, S. and Mann, P. (1999). Structural and sedimentary development of a Neogene transpressional plate boundary between the Caribbean and South American plates in Trinidad and the Gulf of Paria. In

Mann, P., ed., *Caribbean basins: Sedimentary basins of the world* (Volume 4, pp. 495–557). Amsterdam, Netherlands: Elsevier Science B.V.

Barr, K.W. (1965). The Geology of the Toco District, Trinidad, West Indies, Pt. I and II. Overseas Geology and Mineral resources, 8, 4, 379-415 and 9, 1, 1-29.

Bartlett, C., Arkle, J., Weber, J. and Erlich, R. (2021). Provenance of the Northern Range Trinidad Using Detrital Zircon U-Pb Geochronology: Implications for Northern South American River System Paleogeography, Geological Society of America, North-Central Meeting.

Bayet, L., John, T., Agard, P., Gao, J., & Li, J. (2018). Massive sediment accretion at ~80 km depth along the subduction interface: Evidence from the southern Chinese Tianshan. *Geology*, 46(6), 495–498. https://doi.org/10.1130/G40201.1

Beyssac, O., Goffé, B., Chopin, C., & Rouzaud, J. N. (2002). Raman spectra of carbonaceous material in metasediments: a new geothermometer. *Journal of Metamorphic Geology*, 20, 859–871. https://doi.org/10.1046/j.1525-1314.2002.00408.x

Beyssac, O., Goffé, B., Petitet, J. P., Froigneux, E., Moreau, M., & Rouzaud, J. N. (2003). On the characterization of disordered and heterogeneous carbonaceous materials by Raman spectroscopy. *Spectrochimica Acta - Part A: Molecular and Biomolecular Spectroscopy*, 59, 2267–2276. https://doi.org/10.1016/S1386-1425(03)00070-2

Beyssac, O., & Lazzeri, M. (2012). Application of raman spectroscopy to the study of graphitic carbons in the earth sciences. *European Mineralogical Union Notes in Mineralogy*, 12(12), 415–454. https://doi.org/10.1180/EMU-notes.12.12

Beyssac, O., Pattison, D. R. M., & Bourdelle, F. (2019). Contrasting degrees of recrystallization of carbonaceous material in the Nelson aureole, British Columbia and Ballachulish aureole, Scotland, with implications for thermometry based on Raman spectroscopy of carbonaceous material. *Journal of Metamorphic Geology*, 37, 71–95. https://doi.org/10.1111/jmg.12449

Beyssac, O., Simoes, M., Avouac, J. P., Farley, K. A., Chen, Y. G., Chan, Y. C., & Goffé, B. (2007). Late Cenozoic metamorphic evolution and exhumation of Taiwan. Tectonics, 26(6). https://doi.org/10.1029/2006TC002064

Brandon, M. T., Roden-Tice, M. K., & Carver, J. I. (1998). Late Cenozoic exhumation of the Cascadia accretionary wedge in the Olympic Mountains, northwest Washington State. *Bulletin of the Geological Society of America*, 110(8), 985–1009. https://doi.org/10.1130/0016-7606(1998)110<0985:LCEOTC>2.3.CO;2

Burke, K. (1988). Tectonic evolution of The Caribbean. *Annual Reviews in Eath and Planetary Science*, 16, 201–230. https://doi.org/10.1146/annurev.ea.16.050188.001221

Clark, S. A., Sobiesiak, M., Zelt, C. A., Magnani, M. B., Miller, M. S., Bezada, M. J., & Levander, A. (2008). Identification and tectonic implications of a tear in the South American plate at the southern end of the Lesser Antilles. *Geochemistry, Geophysics, Geosystems*, 9(11), 1–10. https://doi.org/10.1029/2008GC002084

Cruz, L., Fayon, A., Teyssier, C., & Weber, J. C. (2007). Exhumation and deformation processes in transpressional orogens: The Venezuelan Paria Peninsula, SE Caribbean-South American plate boundary. *Special Paper of the Geological Society of America*, 434(8), 149–165. https://doi.org/10.1130/2007.2434(08)

De Verteuil, L., Weber, J. C., Ramlal, B., & Gonzalez Alfonso, J. A. (2005). *Geological Map of Trinidad*. Republic of Trinidad and Tobago: Latinum Geological Consultants Limited.

Dighton-Thomas, H. (1935). On some sponges and a coral of Upper Cretaceous Age from Toco Bay, Trinidad, Geological Magazine, 72, 4, 175-179.

Flinch, J. F., Rambaran, V., Ali, W., De Lisa, V. De, Hernández, G., Rodrigues, K., & Sams, R. (1999). Structure of the Gulf of paria pull-apart basin (Eastern Venezuela-Trinidad). In Mann, P., (Ed.) *Sedimentary Basins of the World* (Vol. 4, pp. 477–494). Frisco CO: Elsevier Science. https://doi.org/10.1016/S1874-5997(99)80051-3

Foland, K. A., Speed, R., & Weber, J. C. (1992). Geochronologic studies of the hinterland of the Caribbean orogen of Venezuela and Trinidad. *Geological Society of America Abstracts with Programs*, 24, 148.

Furuichi, H., Ujiie, K., Kouketsu, Y., Saito, T., Tsutsumi, A., Wallis, S. (2015). Vitrinite reflectance and Raman spectra of carbonaceous material as indicators of frictional heating on faults: Constraints from friction experiments. *Earth and Planetary Letters*, 424, 191–200. https://doi.org/10.1016/j.epsl.2015.05.037

Frey, M., Saunders, J., & Schwander, H. (1988). The mineralogy and metamorphic geology of low-grade metasediments, Northern Range, Trinidad. *Journal of the Geological Society, London*, 145, 563–575. https://doi.org/10.1144/gsjgs.145.4.0563

Garciacaro, E., Mann, P., & Escalona, A. (2011). Regional structure and tectonic history of the obliquely colliding Columbus foreland basin, offshore Trinidad and Venezuela. *Marine and Petroleum Geology*, 28, 126–148. https://doi.org/10.1016/j.marpetgeo.2009.08.016

Gennaro, I., Chu, X., Vitale Brovarone, A., Weber, J., Arkle, J. (2021). Peak metamorphic temperatures aquired through Raman Spectroscopy on Carbonaceous Material (RSCM) from the Northern Range, Trinidad. PANGAEA, https://doi.pangaea.de/10.1594/PANGAEA.932772

Giorgis, S., Weber, J. C., Sanguinito, S., Beno, C., & Metcalf, J. (2017). Thermochronology constraints on miocene exhumation in the central range mountains, Trinidad. *Bulletin of the Geological Society of America*, 129(1–2), 171–178. https://doi.org/10.1130/B31363.1

Govers, R., & Wortel, M. J. R. (2005). Lithosphere tearing at STEP faults: Response to edges of subduction zones. Earth and Planetary Science Letters, 236(1–2), 505–523. https://doi.org/10.1016/j.epsl.2005.03.022

Harrison, T. M., Célérier, J., Aikman, A. B., Hermann, J., & Heizler, M. T. (2009). Diffusion of 40Ar in muscovite. *Geochimica et Cosmochimica Acta*, 73(4), 1039–1051. https://doi.org/10.1016/j.gca.2008.09.038

Hoernle, K., Hauff, F., & van den Bogaard, P. (2004). 70 m.y. history (139-69 Ma) for the Caribbean large igneous province. *Geology*, 32(8), 697–700. https://doi.org/10.1130/G20574.1

Imlay, R.W. (1954). Barremian ammonites from Trinidad, B.W.I., Journal of Paleontology, 28, 5, 662-667.

Iwasaki, R., Hirose, M., & Furukawa, Y. (2013). Raman temperature measurements of copper phthalocyanine layer of organic light-emitting diode using bandwidth-temperature relationship. *Japanese Journal of Applied Physics*, 52(5S1), 05DC16.

Kagi, H., Tsuchida, I., Wakatsuki, M., Takahashi, K., Kamimura, N., Iuchi, K., & Wada, H. (1994). Proper understanding of down-shifted Raman spectra of natural graphite: Direct estimation of laser-induced rise in sample temperature. *Geochimica et Cosmochimica Acta*, 58(16), 3527-3530.

Kirlova, M., Toy, V., Rooney, J. S., Giorgetti, C., Gordon, K. C., Collettini, C., Takeshita, T. (2018). Structural disorder of graphite and implications for graphite thermometry. *Solid Earth*, 9, 223–231. https://doi.org/10.5194/se-9-223-2018

Kugler, H. G. (1961). *Geological map and sections of Trinidad*. Zurich, Switzerland: Orell Füssli Arts Graphiques S. A.

Kennan, L., & Pindell, J. L. (2009). Dextral shear, terrane accretion and basin formation in the Northern Andes: Best explained by interaction with a Pacific-derived Caribbean plate? *Geological Society Special Publication*, 328, 487–531. https://doi.org/10.1144/SP328.20

Kouketsu, Y., Mizukami, T., Mori, H., Endo, S., Aoya, M., Hara, H., et al. (2014). A new approach to develop the Raman carbonaceous material geothermometer for low-grade metamorphism using peak width. *Island Arc*, 23, 33–50. https://doi.org/10.1111/iar.12057

Lahfid, A., Beyssac, O., Deville, E., Negro, F., Chopin, C., & Goffé, B. (2010). Evolution of the Raman spectrum of carbonaceous material in low-grade metasediments of the Glarus Alps (Switzerland). *Terra Nova*, 22(5), 354–360. https://doi.org/10.1111/j.1365-3121.2010.00956.x

Levander, A., Bezada, M. J., Niu, F., Humphreys, E. D., Palomeras, I., Thurner, S. M., et al. (2014). Subduction-driven recycling of continental margin lithosphere. *Nature*, 515, 253–256. https://doi.org/10.1038/nature13878

Lünsdorf, N. K., Dunkl, I., Schmidt, B. C., Rantitsch, G., & von Eynatten, H. (2013). Towards a Higher Comparability of Geothermometric Data obtained by Raman Spectroscopy of Carbonaceous Material. Part I: Evaluation of Biasing Factors. *Geostandards and Geoanalytical Research*, 38(1), 73–94. https://doi.org/10.1111/j.1751-908X.2013.12011.x

Luque, F. J., Pasteris, J. D., Wopenka, B., Rodas, M., & Barrenechea, J. F. (1998). Natural Fluid-Deposited Graphite: Mineralogical Characteristics and Mechanisms of Formation. *American Journal of Science*, 298(6), 471–498. https://doi.org/10.2475/ajs.298.6.471

Molli, G., Vitale Brovarone, A., Beyssac, O., & Cinquini, I. (2018). RSCM thermometry in the Alpi Apuane (NW Tuscany, Italy): New constraints for the metamorphic and tectonic history of the inner northern Apennines. *Journal of Structural Geology*, 113, 200–216. https://doi.org/10.1016/j.jsg.2018.05.020

Nakamura, Y., Hara, H., & Kagi, H. (2019). Natural and experimental structural evolution of dispersed organic matter in mudstones: The Shimanto accretionary complex, southwest Japan. *Island Arc*, 28(5), e12318.

Nakamura, Y., Oohashi, K., Toyoshima, T., Satish-Kumar, M., Akai, J. (2015). Strain-induced amorphization of graphite in fault zones of the Hidaka metamorphic belt, Hokkaido, Japan. *Journal of Structural Geology*, 72, 142–161. https://doi.org/10.1016/j.jsg.2014.10.012

Neill, I., Kerr, A., Chamberlain, K. R., Schmitt, A. K., Urbani, F., Hastie, A. R. et al. (2014). Vestiges of the proto-Caribbean seaway: Origin of the Sans Souci volcanic group, Trinidad. *Tectonophysics*, 626, 170–185. https://doi.org/10.1016/j.tecto.2014.04.019

Nijholt, N., & Govers, R. (2015). The role of passive margins on the evolution of Subduction-Transform Edge Propagators (STEPs). *Journal of Geophysical Research: Solid Earth*, 120, 7203–7230. https://doi.org/10.1002/2015JB012202

Pindell, J., & Kennan, L. (2001). Processes and Events in the Terrane Assembly of Trinidad and Eastern Venezuela. In *Petroleum Systems of Deep-Water Basins: Global and Gulf of Mexico Experience: 21st Annual* (159–192). Red Hook, NY: Curran Associates Inc. https://doi.org/10.5724/gcs.01.21.0159

Pindell, J. & Kennan, L. (2007). Cenozoic Kinematics and Dynamics of Oblique Collision Between two Convergent Plate Margins: The Caribbean-South America Collision in Eastern Venezuela, Trinidad and Barbados. In *Transactions of GCSSEPM 27th Annual Bob F. Perkins Research Conference*, 458-553. https://doi.org/10.5724/gcs.07.27.0458

Pindell, J. & Kennan, L. (2009). Tectonic evolution of the Gulf of Mexico, Caribbean and northern South America in the mantle reference frame: an update. In *Geological Society London, Special Publications*, 328, 1–55. https://doi.org/10.1144/SP328.1

Potter, H. C. (1968). A preliminary account of the stratigraphy and structure of the eastern part of the Northern Range, Trinidad. In *Transactions of the Fourth Caribbean Geological Conference,* Trinidad, 15–20.

Potter, H. C. (1973). The overturned anticline of the Northern Range of Trinidad near Port of Spain. *Journal of the Geological Society*, 129, 133–137. http://dx.doi.org/10.1144/gsjgs.129.2.0133

Rahl, J. M., Anderson, K. M., Brandon, M. T., & Fassoulas, C. (2005). Raman spectroscopic carbonaceous material thermometry of low-grade metamorphic rocks: Calibration and application to tectonic exhumation in Crete, Greece. *Earth and Planetary Science Letters*, 240(2), 339–354. https://doi.org/10.1016/j.epsl.2005.09.055

Robertson, P., & Burke, K. (1989). Evolution of southern Caribbean plate boundary, vicinity of Trinidad and Tobago. *American Association of Petroleum Geologists Bulletin*, 73(4), 490–509. https://doi.org/10.1306/44b49fdd-170a-11d7-8645000102c1865d

Rogiers, B., Huysmans, M., Vandenberghe, N., Verkeyn, M. (2014). Demonstrating large-scale cooling in a Variscan terrane by coupled groundwater and heat flow modelling. *Geothermics*, 51, 71–90. http://dx.doi.org/10.1016/j.geothermics.2013.10.014

Rumble, D. (2014). Hydrothermal graphitic carbon. *Elements*, 10(6), 427–433. https://doi.org/10.2113/gselements.10.6.427

Russo, R. M., & Speed, R. C. (1992). Oblique collision and tectonic wedging of the South American continent and Caribbean terranes. *Geology*, 20(5), 447–450. https://doi.org/10.1130/0091-7613(1992)020<0447:OCATWO>2.3.CO;2

Russo, R. M., & Speed, R. C. (1994). Spectral analysis of gravity anomalies and the architecture of tectonic wedging, NE Venezuela and Trinidad. *Tectonics*, 13(3), 613–622. https://doi.org/10.1029/94TC00052

Simoes, M., Avouac, J. P., Beyssac, O., Goffé, B., Farley, K. A., & Chen, Y. G. (2007). Mountain building in Taiwan: A thermokinematic model. *Journal of Geophysical Research: Solid Earth*, 112(11), 1–25. https://doi.org/10.1029/2006JB004824

Saunders, J.B. (1972). Recent paleontological results from the Norther Range of Trinidad, Proceedings on the Sixth Caribbean Geological Conference, Caracas, 455-460.

Saunders, J. B., Roberts, C., Ali, W. M., Eggerston, B. (1997). *Geological Map, Trinidad and Tobago*. Trinidad and Tobago: Ministry of Energy and Energy Resources.

Spath, L.F. (1939). On some Tithonian ammonites from the Northern Range of Trinidad, British West Indies Geological Magazine, 76, 898, 187-198.

Speed, R. C. (1985). Cenozoic Collision of the Lesser Antilles Arc and Continental South America and the Origin of the El Pilar Fault. *Tectonics*, 4(1), 41–69. https://doi.org/10.1029/TC004i001p00041

Speed, R.C., Sharp, W.D., and Foland, K.A., (1997). Late Paleozoic granitiod gneiss of northeastern Venezuela and the North American-Gondwana collision zone, Journal of Geology, 105(4), 457–470.

Teyssier, C., Tikoff, B., Weber, J. (2002). Attachment between brittle and ductile crust at wrenching plate boundaries. *EGU Stephan Mueller Special Publication Series*, 1, 75–91.

Trechmann, C.T. (1935). Fossils from the Northern Range of Trinidad, Geological Magazine, 72, 850, 166-175.

Vitale Brovarone, A., & Agard, P. (2013). True metamorphic isograds or tectonically sliced metamorphic sequence? New high-spatial resolution petrological data for the New Caledonia case study. *Contributions to Mineralogy and Petrology*, 166(2), 451–469. https://doi.org/10.1007/s00410-013-0885-2

Vitale Brovarone, A., Beyssac, O., Malavieille, J., Molli, G., Beltrando, M., & Compagnoni, R. (2013). Stacking and metamorphism of continuous segments of subducted lithosphere in a high-pressure wedge: The example of Alpine Corsica (France). *Earth-Science Reviews*, 116(1), 35–56. https://doi.org/10.1016/j.earscirev.2012.10.003

Wadge, G & Macdonald, R. (1985). Cretaceous tholeiites of the southern continental margin of South America: the Sans Souci Formation of Trinidad. *Journal of the Geological Society of London*, 142, 297–308. https://doi.org/10.1144/gsjgs.142.2.0297

Wang, Y., Alsmeyer, D. C., McCreery, R. L. (1990). Raman spectroscopy of carbon materials: Structural basis of observed spectra. *Chemical Materials*, 2, 557–563.

Weber, J. C. (2009). Neotectonics in the Trinidad and Tobago, West Indies segment of the Caribbean-South American plate boundary. *Occasional Papers of the Geological Institute of Hungary*, 204, 21–29.

Weber, J. C., & Arkle, J. (2015). *Field Trip Field Guide Trinidad's Northern Range: "reversal of fortune": Bedrock Structure and Metamorphic Geology, and Tectonic Geomorphology*. Port-of-Spain, Trinidad: 20th Caribbean Geological Conference.

Weber, J. C., Dixon, T. H., DeMets, C., Ambeh, W. B., Jansma, P., Mattioli, G., et al. (2001). GPS estimate of relative motion between the Caribbean and South American plates, and geologic implications for Trinidad and Venezuela. *Geology*, 29(1), 75–78. https://doi.org/10.1130/0091-7613(2001)029<0075:GEORMB>2.0.CO;2

Weber, J. C., Ferrill, D. A., & Roden-Tice, M. K. (2001). Calcite and quartz microstructural geothermometry of low-grade metasedimentary rocks, Northern Range, Trinidad. Journal of Structural Geology, 23(1), 93–112. https://doi.org/10.1016/S0191-8141(00)00066-3

Weber, J. C., H. Geirsson, J. L. Latchman, K. Shaw, P. La Femina, S. Wdowinski, M. Higgins, C. Churches, and E. Norabuena (2015), Tectonic inversion in the Caribbean-South American plate boundary: GPS geodesy, seismology, and tectonics of the M_W 6.7 22 April 1997 Tobago earthquake, Tectonics, 34, 1181–1194, doi:10.1002/2014TC003665.

Weber, J. C., Geirsson, H., La Femina, P., Robertson, R., Churches, C., Shaw, K., et al. (2020). Fault Creep and Strain Partitioning in Trinidad-Tobago: Geodetic Measurements, Models, and Origin of Creep. *Tectonics*, 39(1), e2019TC005530. https://doi.org/10.1029/2019TC005530

Willett, S., Beaumont, C., & Fullsack, P. (1993). Mechanical model for the tectonics of doubly vergent compressional orogens. *Geology*, 21(4), 371–374. https://doi.org/10.1130/0091-7613(1993)021<0371:MMFTTO>2.3.CO;2

Wopenka, B., & Pasteris, J. D. (1993). Structural characterization of kerogens to granulite-facies graphite: Applicability of Raman microprobe spectroscopy. American Mineralogist, 78(5–6), 533–557.

Table 1. Rock Type, Location, and RSCM Temperatures of Northern Range Samples

Sample	Spectro-meter	Lithology	UTM X coordinate[a]	UTM Y coordinate[a]	5-Peak Spectra Temperature (SE)[f]		3-Peak Spectra Temperature (SE)[g]		**RSCM Temperature (SE)[e]**		FWHM-D1 Temperature (SE)[h]		FWHM-D2 Temperature (SE)[h]	
DT-93-1[b]	-	Phyllite	672200	1189900	-	-	-	-	**-**	**-**	-	-	-	-
145	UNITO	Schist	672500	1178400			348	2.9	**348**	**2.9**	362	3.6	277	18.3
HT-161	ROM	Phyllite	672500	1178400	341	4.0	355	2.1	**347**	**4.7**	360	3.4	383	3.6
CF-94-1	ROM	Marble	672698	1178373			353	1.8	**353**	**1.8**	367	2.6	332	6.8
T94-3	ROM	Slate	723638	1198298	325	4.4			**325**	**4.4**	287	5.0	320	1.1
T97-MAT3	ROM	Slate	706235	1196714	339	2.9			**339**	**2.9**	298	2.1	322	0.9
M-3	UNITO	Schist	671697	1189674	*1 outlier*		461	4.7	**461**	**4.7**	-	-	-	-
	ROM	Schist	671697	1189674			447	3.6	**447**	**3.6**	-	-	-	-
M-4	UNITO	Schist	671697	1189674	*1 outlier*		497	7.9	**497**	**7.9**	-	-	-	-
	ROM	Schist	671697	1189674			492	10.6	**492**	**10.6**	-	-	-	-
Ar-17	ROM	Metasandstone	683682	1193264	364	3.9			**364**	**3.9**	334	3.5	310	3.6
LC-91a	UNITO	Metasandstone	675697	1192174			413	3.6	**413**	**3.6**	-	-	-	-
T90-9b	ROM	Phyllite	672820	1178826			340	1.4	**340**	**1.4**	354	3.1	298	7.1
LN-94-1	UNITO	Metacarbonate	721934	1197921	327	3.1			**327**	**3.1**	243	5.3	256	11.7
	ROM	Metacarbonate	721934	1197921	272	3.5			**272**	**3.5**	270	5.8	292	9.1
SC-2	UNITO	Marble	666223	1185430			465	8.6	**465**	**8.6**	-	-	-	-
T94-1	UNITO	Metacarbonate	723497	1198074	322	2.7			**322**	**2.7**	227	7.9	323	5.5
	ROM	Metacarbonate	723497	1198074	302	2.5			**302**	**2.5**	245	3.5	360	3.5
SC-2b	UNITO	Marble	669482	1189870	*1 outlier*		449	4.1	**449**	**4.1**	-	-	-	-
MV-94-3	ROM	Metacarbonate	717297	1197675	310	3.5			**310**	**3.5**	263	1.6	319	7.2
PG-94-5[c]	ROM	Metacarbonate	650597	1180273			315[c]		**315[c]**		314[c]		287[c]	
93-T-CB	UNITO	Marble	679302	1194346	*3 outliers*		366	4.6	**366**	**4.6**	354	2.4	248	8.9
MAT-1	ROM	Slate	704866	1196982	341	4.1	*1 outlier*		**341**	**4.1**	292	3.2	320	3.7
CB-2a	UNITO	Marble	678698	1195474	348[d]		344	1.2	**344**	**1.2**	349	2.1	233	10.9
	ROM	Marble	678698	1195474			341	1.4	**341**	**1.4**	366	2.3	302	5.8
DT-93	UNITO	Schist	672763	1189887			454	2.9	**454**	**2.9**	-	-	-	-
	ROM	Schist	672763	1189887			453	3.3	**453**	**3.3**	-	-	-	-
MB-93-1	ROM	Schist	650900	1187570			444	5.2	**444**	**5.2**	-	-	-	-
LC-91b	UNITO	Schist	676033	1192116			422	3.9	**422**	**3.9**	-	-	-	-
LC-3	ROM	Phyllite	661869	1180984			410	2.2	**410**	**2.2**	-	-	-	-
NR-1	UNITO	Metasandstone	720092	1185918			338	0.3	**337**	**2.2**	343	2.0	244	7.2
	ROM	Metasandstone	720092	1185918	336	4	341	1.1	**342**	**1.1**	355	1.5	287	3.8
NR-2 (-5)	UNITO	Slate	724652	1192884	351	1.5	340	***	**350**	**4.5**	311	1.9	311	4.1
NR-3 (-1)	UNITO	Metasandstone	720092	1185918	327	1.3	335	0.3	**329**	**3.7**	318	5.5	174	10.8

[a] UTM coordinates are in Zone 20.

[b] Sample DT-93-1 was unable to be analyzed due to a lack of carbonaceous material.

[c] Sample PG-94-5 has a temperature based on one spectrum as all other spectra collected contained large calcite peaks and could not be fit accurately.

[d] One spectrum only.

[e] These temperatures are calculated using the Aoya et al. (2010) or Lahfid et al. (2010) calibrations. In samples displaying both 3- and 5-band spectra both calibrations were used, with the reported value representing the average temperature of all spectra associated with that sample (exculding outliers). Consult the supplementary material for a full breakdown of the calibrations used for each spectrum.

[f] Aoya et al. (2010).

[g] Lahfid et al. (2010).

[h] Kouketsu et al. (2014).

Figure Captions

Figure 1: a) Schematic tectonic map of the eastern Caribbean showing major plate boundaries. Trinidad (grey) is currently located on the right-lateral strike-slip transform boundary along the southern edge of the Caribbean Plate. PC – Paria cluster of seismicity. b) Map of Trinidad emphasizing the Northern Range study area (grey) and major faults in the region. The active faults (Central Range and Los Bajos faults, bold lines) accommodate most of the present plate motion between the Caribbean and South America (Weber, Dixon, et al., 2001). The Northern Range is bound by the inactive North Coast and Sub-Tobago Terrane fault zones to the north and Arima Fault to the south. The El Pilar Fault zone is active in eastern Venezuela but is inactive or not present in Trinidad. c) Cross section of the subduction-transform edge propagator (STEP) plate boundary and associated lithospheric tear located below the Caribbean Plate. The subduction-transform boundary is located at the letter "S" while the site of active and deep tearing is located at the Paia Cluster, which is a major zone of earthquakes in the area as a result of the slab tear (Russo & Speed, 1992). Modified after Arkle et al. (2021).

Figure 2: Simplified geologic map from De Verteuil et al. (2005) of the Northern Range showing metamorphic units, sample localities, and relict fossil ages. Apart from the Sans Souci Metabasalt, all lithologic units are metamorphosed from sedimentary protoliths (Frey et al., 1988), with relict fossil ages only available from eastern block, lower-grade units (Dighton-Thomas, 1935; Imlay, 1954; Kugler, 1961; Saunders, 1972; Spath, 1939; Trechmann, 1935). A total of 26 RSCM samples were collected and grouped into six representative rock types. Sample distribution was based on obtaining a broad range of compositions and textures. PS – Port of Spain; CP – Chupara Point; VV – Verdant Vale; M – Maturita; T – Toco.

Figure 3: Photomicrographs of petrographic thin sections displaying representative features of each rock type. a) calcite (Cal) marble with carbonaceous material (Gr) concentrated into dark bands; b) calcite (Cal) vein in a metacarbonate rock indicating late extensional brittle deformation and infilling via precipitation from a CO_2-rich fluid; c) low-grade metacarbonate marble displaying primary sedimentary structures (ooids) which have been moderately strained by ductile deformation but have not been recrystallized; d) quartz-mica (Qz-Ms) schist with foliation and minor calcite, likely representing a sandstone protolith; e) mica-rich (Ms) phyllite displaying crenulation after multiple deformation events; f) radial growth of carbonaceous material (CM) superimposed on schistosity; g) metasandstone with minor chlorite (Chl), muscovite, and quartz (Qz); h) folded quartz (Qz)- and CM (Gr)-rich layers in a metasandstone; i) slate rich in carbonaceous material, quartz (Qz), and mica (Ms). PPL: plane-polarized light, XPL: cross-polarized light, RL: reflected light.

Figure 4: a) Backscattered electron (BSE) image of a foliated slate. The dolomite (dol) in the sample has a euhedral shape whereas the calcite (cc) appears more subhedral-anhedral, indicating a lack of equilibrium between the two phases. Pyrite (py) framboids are also present. b) $CaCO_3$-$MgCO_3$-$FeCO_3$

phase diagrams calculated for different temperatures (Anovitz & Essene, 1987), with carbonate compositions plotted in red.

Figure 5: Peak-fitted Raman spectra of (a) high- and (b) low- temperature samples. The high-temperature spectra are fit with Voigt bands while Lorentzian bands are used for the low-temperature spectrum; the area ratios between these bands are used to calculate the peak metamorphic temperature of a sample (Aoya et al., 2010; Lahfid et al., 2010). c) Raman spectra showing decreasing band complexity, correlating to increasing crystallinity and peak metamorphic temperature, from bottom to top. The temperatures shown are calculated using the [1]Lahfid et al. (2010) and [2]Aoya et al. (2010) calibrations.

Figure 6: Inter-instrument error between Raman spectrometers at UNITO and the ROM. The low-temperature calibrations of Lahfid et al. (2010) and Kouketsu et al. (2014) show a lower reproducibility than the high-temperature calibration of Aoya et al. (2010). Inset: variability between the two calibrations of Kouketsu et al. (2014) which are up to 100 °C.

Figure 7: a) RSCM results given in °C plotted on a geologic map of Trinidad overlying topographic (radar) data. The abrupt temperature change in the central Northern Range is marked by a major lithologic boundary along the previously mapped Chupara Fault (Kugler, 1961; De Verteuil et al., 2005). The temperatures shown are calculated using the Aoya et al. (2010) and Lahfid et al. (2010) calibrations. b) Temperature (± 1 s.e.) for samples along the north coast of the Northern Range calculated using a variety of RSCM calibrations. Lower temperature samples from the southwestern Chancellor Schist are excluded as they are separated from the higher temperature samples by the E-W trending Arima Fault. Average temperatures (1σ) of the eastern and western blocks are displayed as the blue-shaded regions.

Figure 8: Cooling history of the a) eastern and b) western Northern Range modified from the QTQt bedrock cooling models of Arkle et al. (2021). Timing of peak metamorphism is estimated by $^{40}Ar/^{39}Ar$ ages through the Northern Range (Speed et al., 1997, Weber & Arkle, 2015). In the east, the cooling path following peak metamorphic temperature, and possibly its timing, remains largely unconstrained due to the disparity between un-reset ZFT ages and high RSCM temperatures, potentially indicating a short-lived thermal event. Dark and light grey lines are the expected cooling histories of the high and low elevation samples, respectively, with the shaded regions representing a 95% confidence interval (Arkle et al., 2021).

Figure 9: Cartoon showing tectonic evolution of the Northern Range and Araya-Paria, Venezuela, metamorphic hinterland, modified from Arkle et al. (2021). a) Following Jurassic-Cretaceous rifting, the area was dominated by passive margin deposition of sediment along continental South America. b) Oblique plate collision led to peak metamorphism and thrust faulting in the Northern Range in the late Oligocene. This time marks the inception of foreland and hinterland structures and of hinterland

metamorphism. c) A transition to strike-slip plate motion between the Caribbean and South American plates produced structures such as the Gulf of Paria pull-apart basin. Eastward propagation of the STEP edge induced greater exhumation of the western Northern Range upon its arrival in Trinidad, which was accommodated by the Chupara Fault. d) Continued STEP propagation along the plate boundary led to an inversion in Northern Range exhumation and late Pliocene to recent surface uplift, with subsidence currently dominant in the west as the east experiences surface uplift (e.g., Arkle et al. 2017, 2021). NR – Northern Range; SdI – Serranía del Interior; MB – Maturin Basin; CR – Central Range; SR – Southern Range; CF – Chupara Fault; NCFZ – Northern Coastal fault zone; EPFZ – El Pilar Fault zone; CB – Columbus Basin.

Figure S1: Plots of nominal temperatures calculated using 3- (Aoya et al., 2010; square symbols) and 5-band (Lahfid et al., 2010; plus signs) calibrations against the centers of fitted G bands. The G band of fully ordered graphite (1582 cm^{-1}; Wang et al., 1990) is labeled by dashed lines for reference. The analyses at UNITO and ROM are denoted by black and blue colors, respectively.

Figure 1

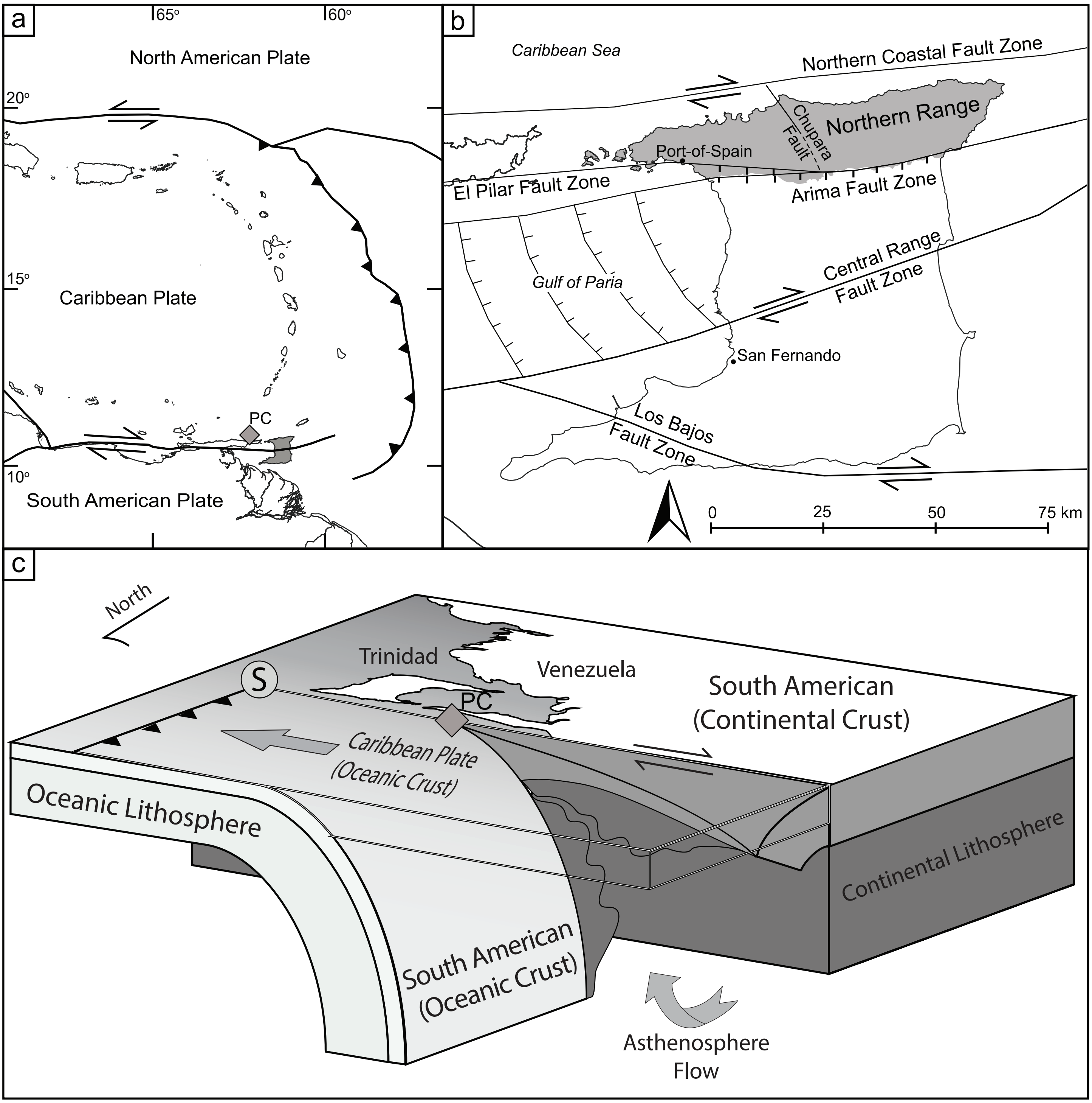
a
65°
60°
North American Plate
20°
15°
Caribbean Plate
PC
10°
South American Plate
b
Caribbean Sea
Northern Coastal Fault Zone
Northern Range
Chupara Fault
Port-of-Spain
El Pilar Fault Zone
Arima Fault Zone
Gulf of Paria
Central Range Fault Zone
San Fernando
Los Bajos Fault Zone
0
25
50
75 km
c
North
Trinidad
Venezuela
S
PC
South American (Continental Crust)
Caribbean Plate (Oceanic Crust)
Oceanic Lithosphere
Continental Lithosphere
South American (Oceanic Crust)
Asthenosphere Flow

Figure 2

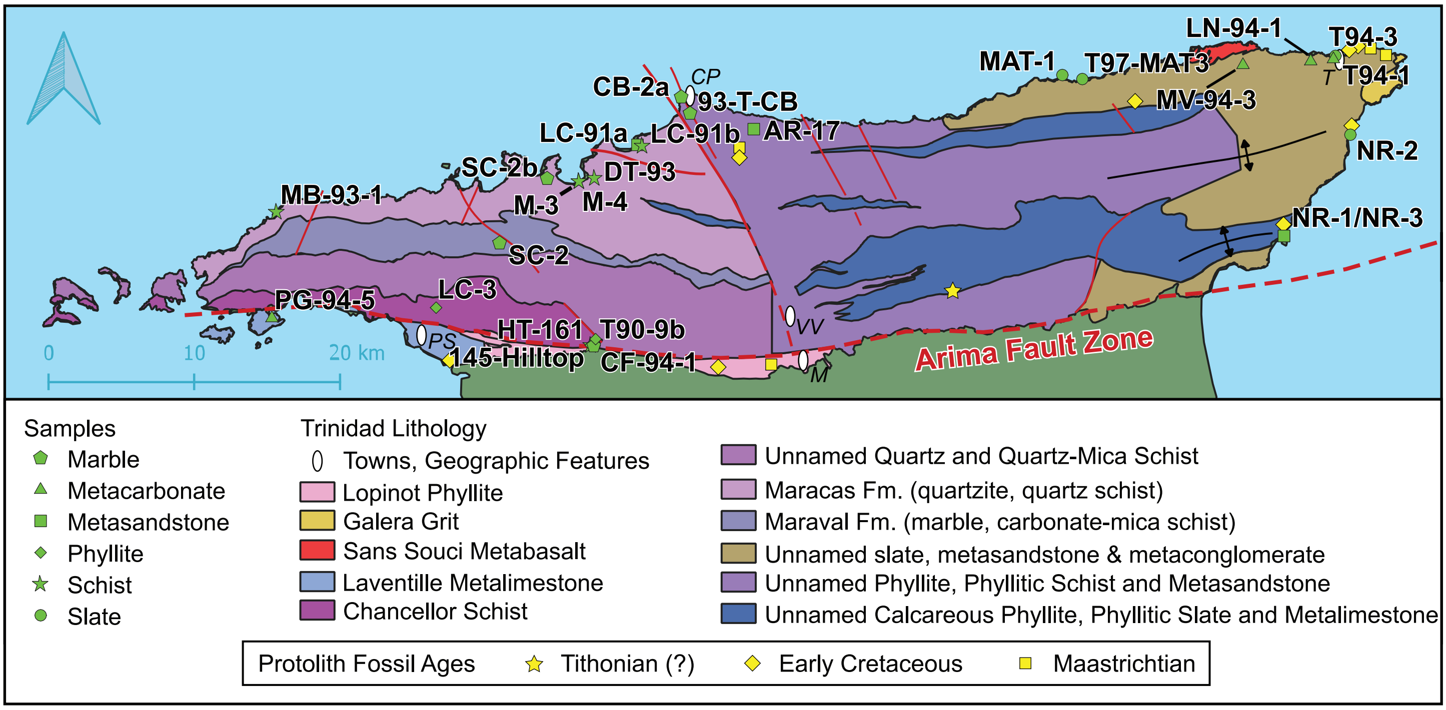

LN-94-1
T94-3
MAT-1
T97-MAT3
T94-1
CB-2a
CP
93-T-CB
MV-94-3
LC-91a
LC-91b
AR-17
NR-2
SC-2b
DT-93
MB-93-1
M-3
M-4
NR-1/NR-3
SC-2
PG-94-5
LC-3
HT-161
T90-9b
PS
145-Hilltop
CF-94-1
VV
M
T
Arima Fault Zone
0
10
20 km
Samples
Marble
Metacarbonate
Metasandstone
Phyllite
Schist
Slate
Trinidad Lithology
Towns, Geographic Features
Lopinot Phyllite
Galera Grit
Sans Souci Metabasalt
Laventille Metalimestone
Chancellor Schist
Unnamed Quartz and Quartz-Mica Schist
Maracas Fm. (quartzite, quartz schist)
Maraval Fm. (marble, carbonate-mica schist)
Unnamed slate, metasandstone & metaconglomerate
Unnamed Phyllite, Phyllitic Schist and Metasandstone
Unnamed Calcareous Phyllite, Phyllitic Slate and Metalimestone
Protolith Fossil Ages
Tithonian (?)
Early Cretaceous
Maastrichtian

Figure 3

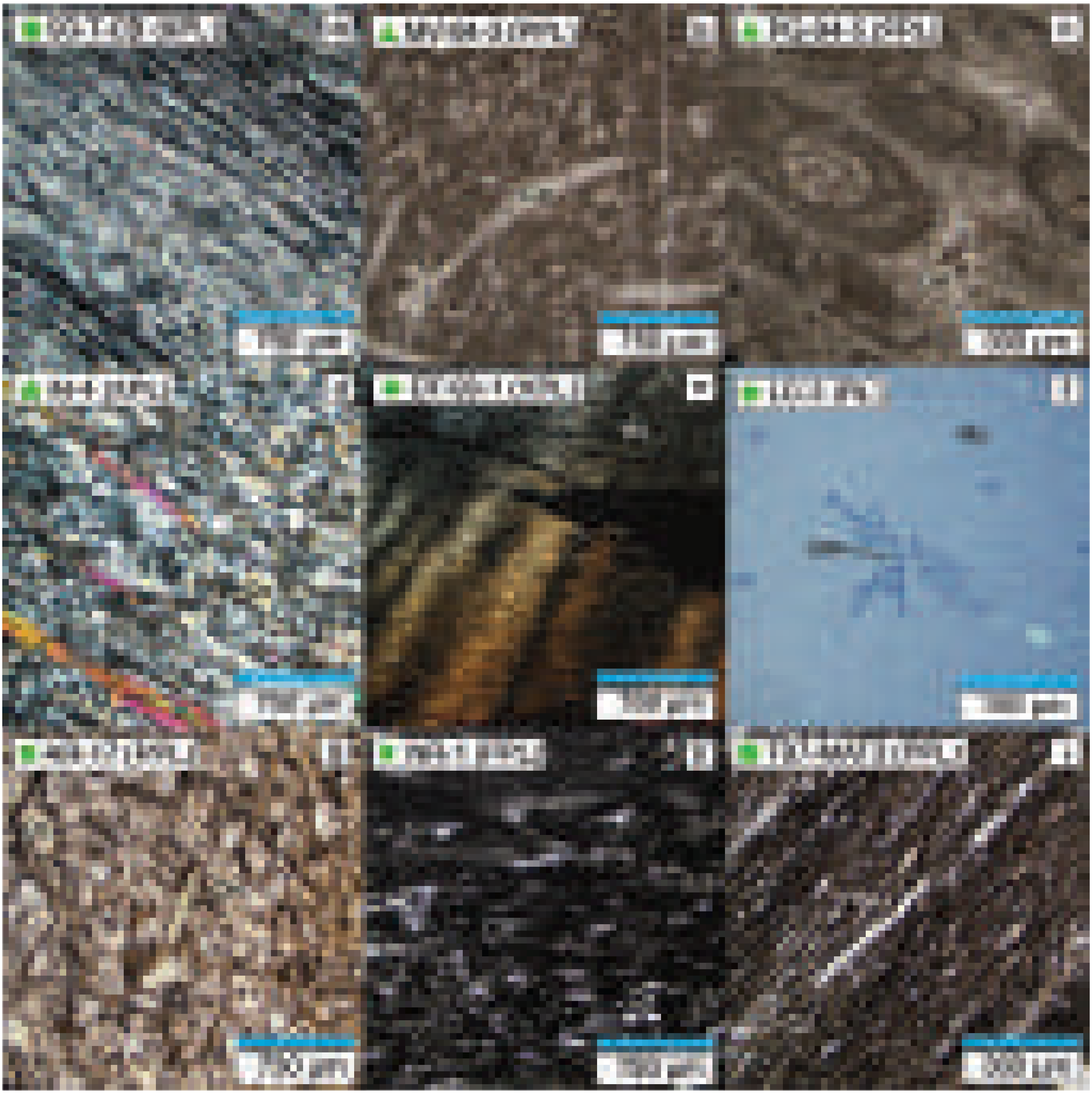

Figure 4

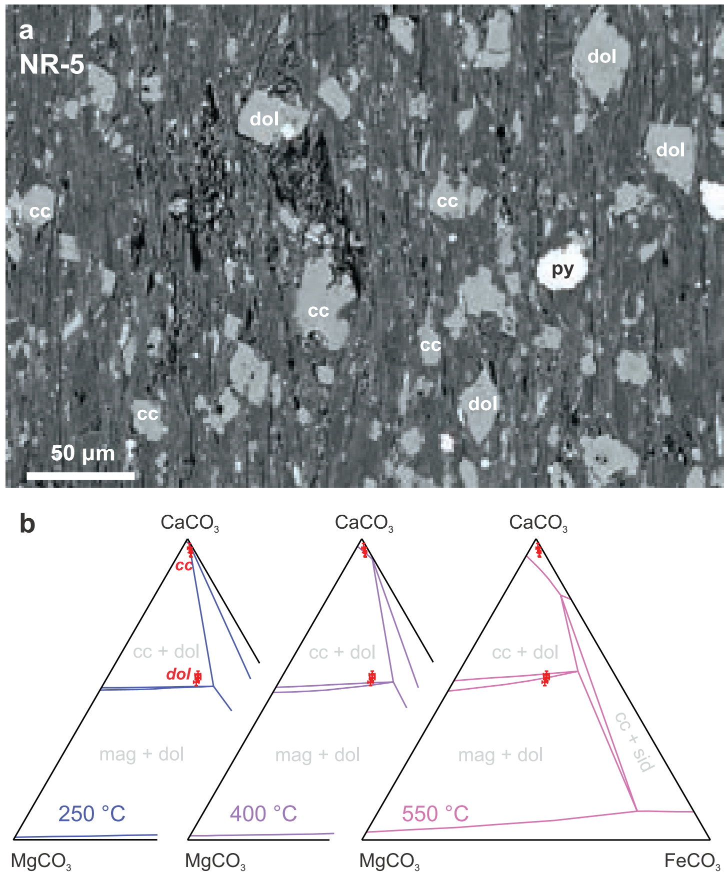
a
NR-5
dol
dol
dol
cc
cc
py
cc
cc
dol
cc
50 µm
b
CaCO$_3$
cc
cc + dol
dol
mag + dol
250 °C
MgCO$_3$
CaCO$_3$
cc + dol
mag + dol
400 °C
MgCO$_3$
CaCO$_3$
cc + dol
cc + sid
mag + dol
550 °C
MgCO$_3$
FeCO$_3$

Figure 5

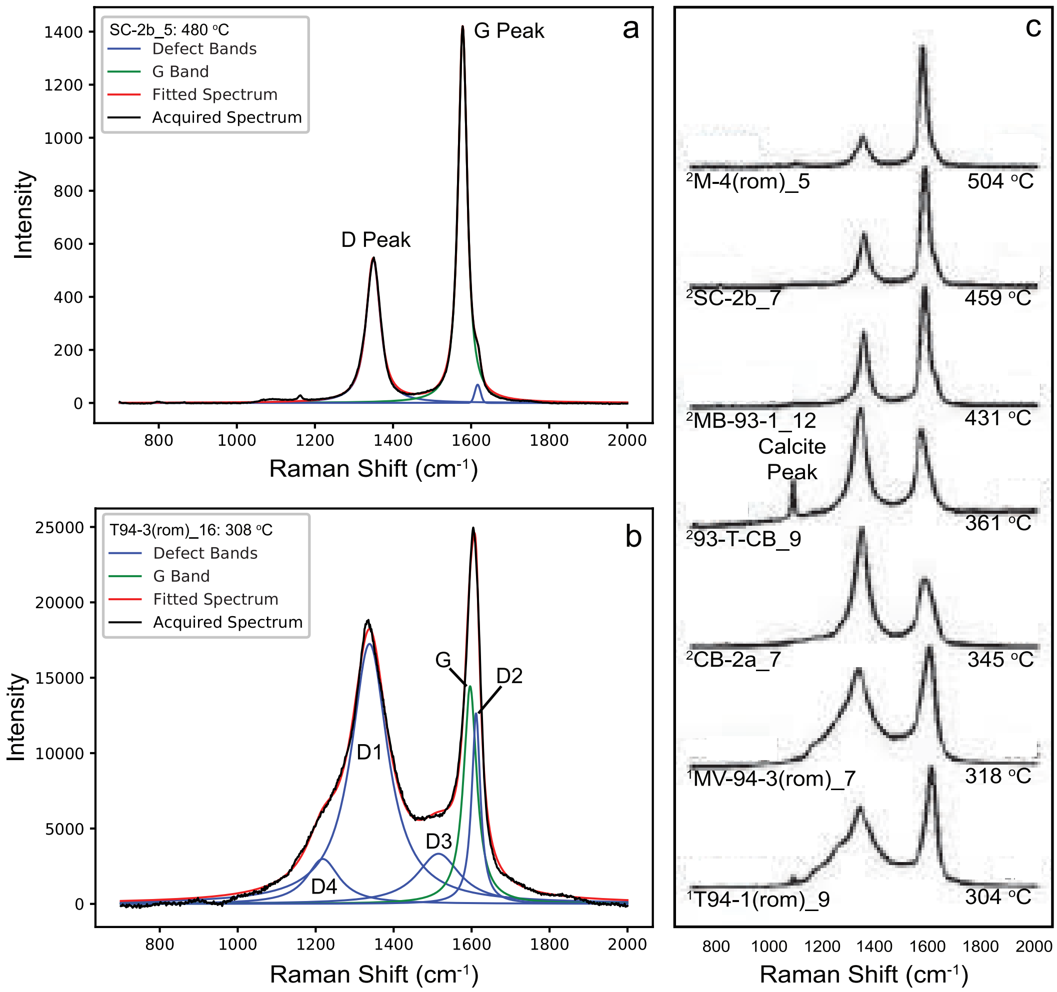

SC-2b_5: 480 °C
Defect Bands
G Band
Fitted Spectrum
Acquired Spectrum
G Peak
a
D Peak
Intensity
Raman Shift (cm-1)
T94-3(rom)_16: 308 °C
Defect Bands
G Band
Fitted Spectrum
Acquired Spectrum
b
G
D2
D1
D3
D4
Intensity
Raman Shift (cm-1)
c
2M-4(rom)_5
504 °C
2SC-2b_7
459 °C
2MB-93-1_12
431 °C
Calcite Peak
293-T-CB_9
361 °C
2CB-2a_7
345 °C
1MV-94-3(rom)_7
318 °C
1T94-1(rom)_9
304 °C
Raman Shift (cm-1)

Figure 6

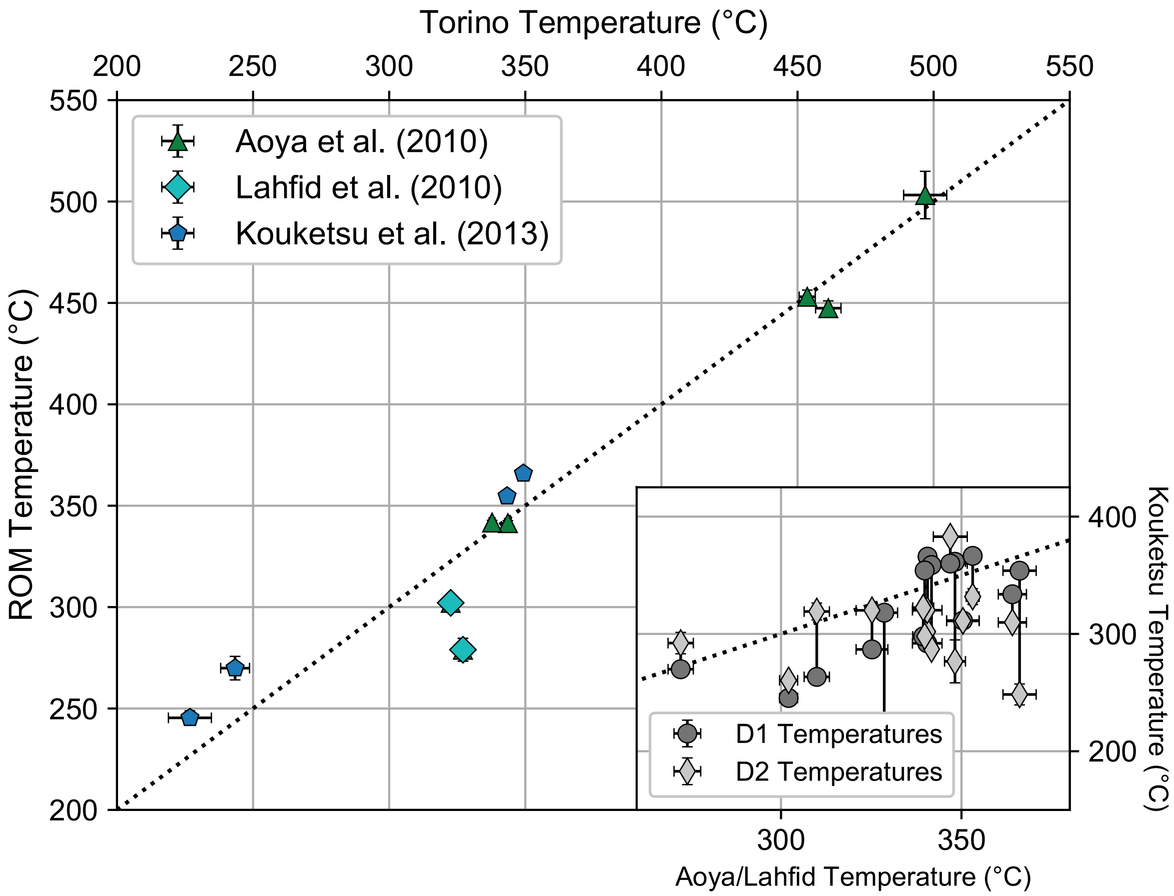

Torino Temperature (°C)
200
250
300
350
400
450
500
550
ROM Temperature (°C)
Aoya et al. (2010)
Lahfid et al. (2010)
Kouketsu et al. (2013)
D1 Temperatures
D2 Temperatures
Kouketsu Temperature (°C)
Aoya/Lahfid Temperature (°C)

Figure 7

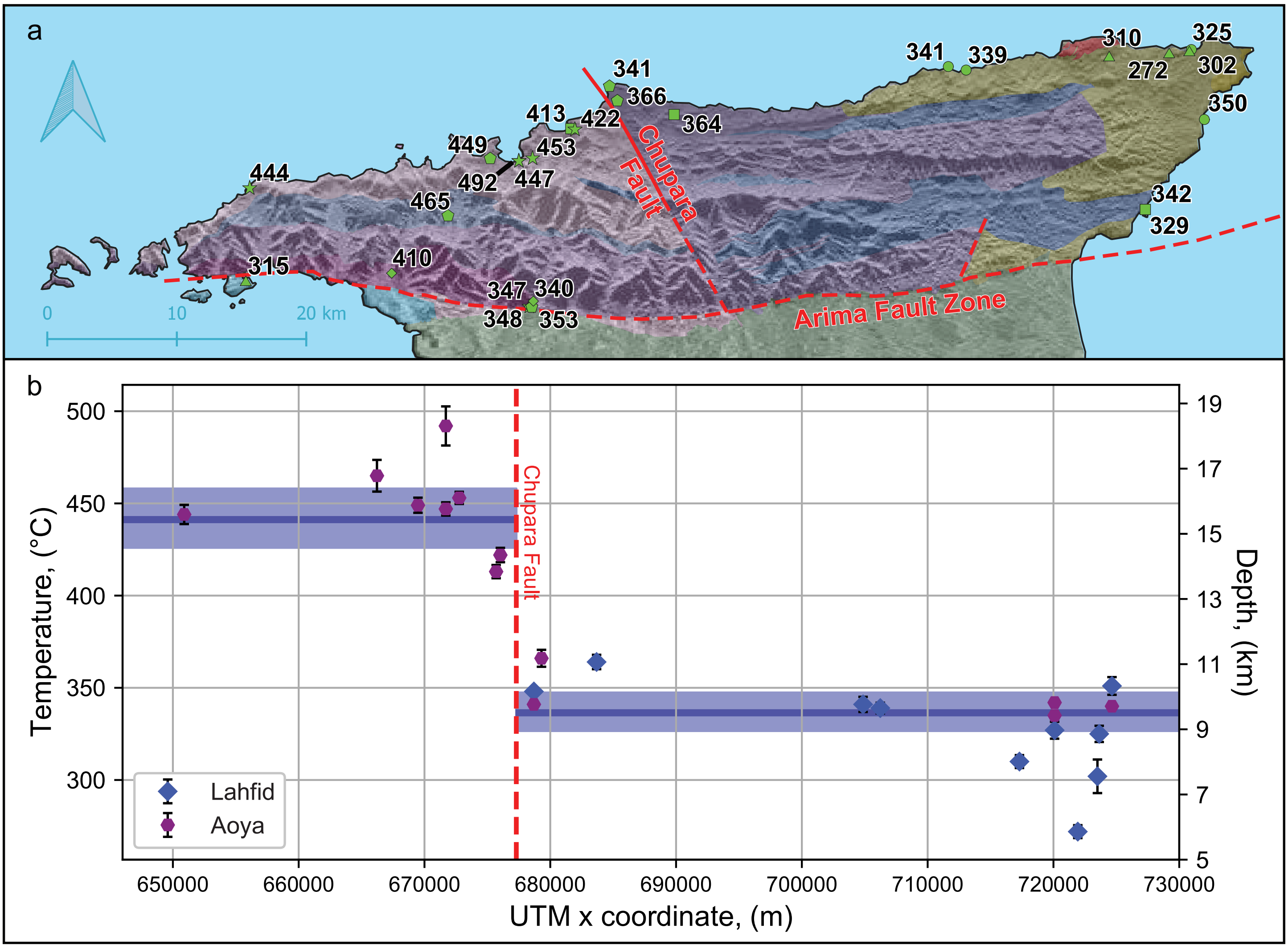

a
341
339
310
325
272
302
350
341
366
364
413
422
449
453
492
447
444
465
342
329
315
410
347
340
348
353
Chupara Fault
Arima Fault Zone
0
10
20 km
b
Temperature, (°C)
Depth, (km)
UTM x coordinate, (m)
Chupara Fault
Lahfid
Aoya

Figure 8

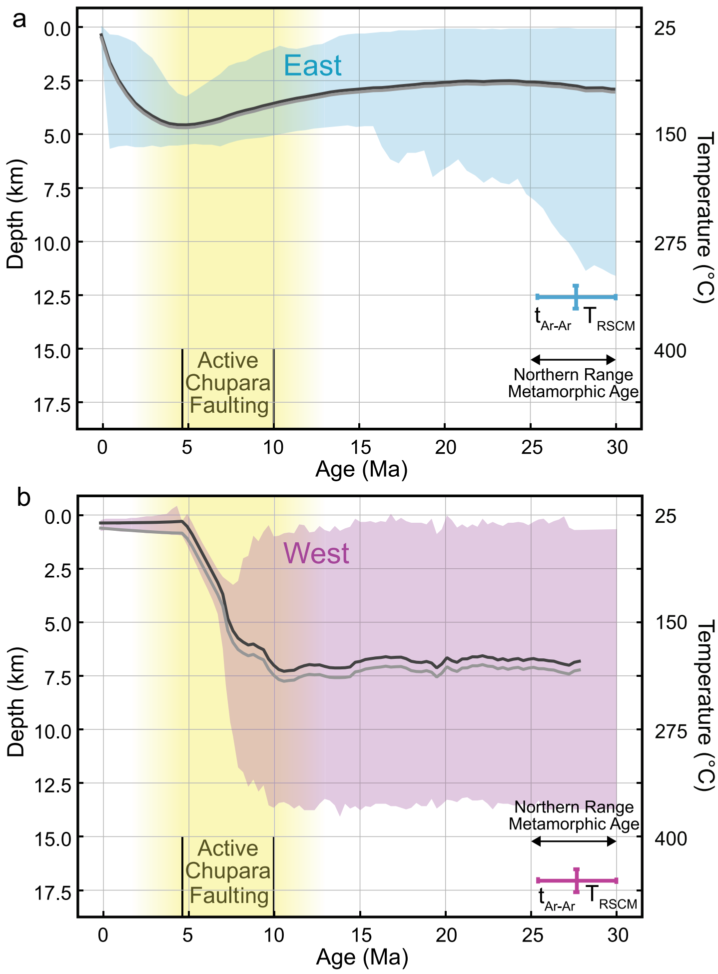
a
East
Depth (km)
Temperature (°C)
Age (Ma)
Active Chupara Faulting
t_{Ar-Ar} T_{RSCM}
Northern Range Metamorphic Age
b
West
Depth (km)
Temperature (°C)
Age (Ma)
Active Chupara Faulting
Northern Range Metamorphic Age
t_{Ar-Ar} T_{RSCM}

Figure 9

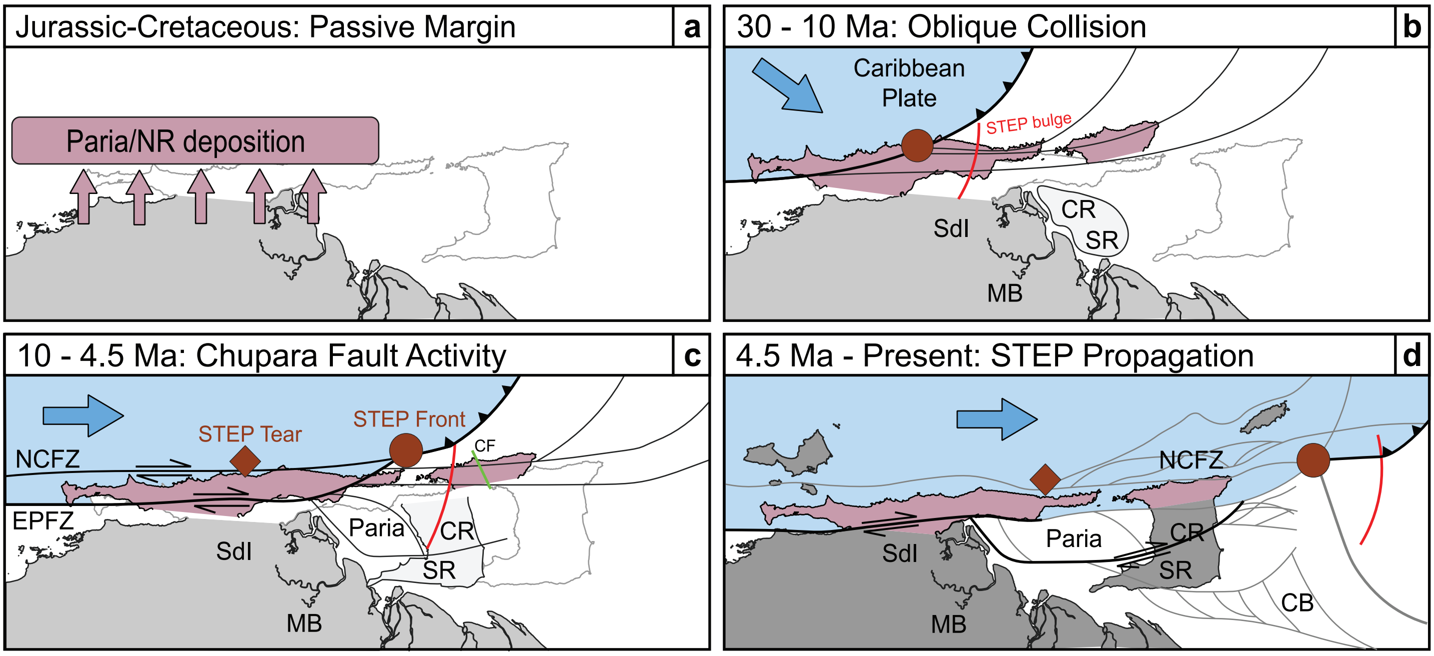

Jurassic-Cretaceous: Passive Margin
a
Paria/NR deposition
30 - 10 Ma: Oblique Collision
b
Caribbean Plate
STEP bulge
CR
SR
SdI
MB
10 - 4.5 Ma: Chupara Fault Activity
c
STEP Tear
STEP Front
CF
NCFZ
EPFZ
Paria
CR
SR
SdI
MB
4.5 Ma - Present: STEP Propagation
d
NCFZ
Paria
CR
SR
SdI
MB
CB

Figure S1

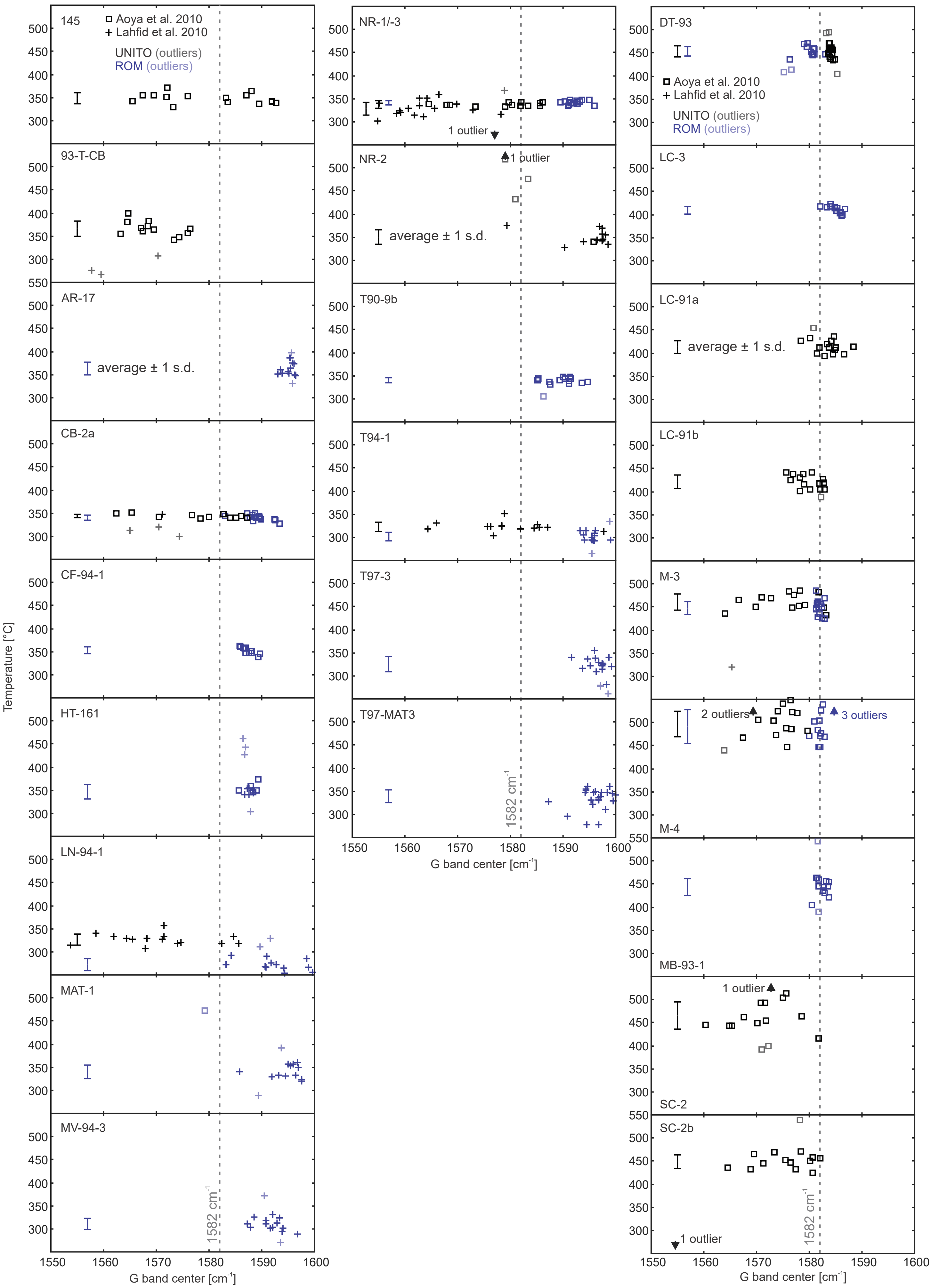

145
Aoya et al. 2010
Lahfid et al. 2010
UNITO (outliers)
ROM (outliers)
93-T-CB
AR-17
average ± 1 s.d.
CB-2a
CF-94-1
HT-161
LN-94-1
MAT-1
MV-94-3
NR-1/-3
1 outlier
NR-2
1 outlier
average ± 1 s.d.
T90-9b
T94-1
T97-3
T97-MAT3
DT-93
Aoya et al. 2010
Lahfid et al. 2010
UNITO (outliers)
ROM (outliers)
LC-3
LC-91a
average ± 1 s.d.
LC-91b
M-3
2 outliers
3 outliers
M-4
MB-93-1
1 outlier
SC-2
SC-2b
1 outlier
1582 cm-1
Temperature [°C]
G band center [cm-1]
1550
1560
1570
1580
1590
1600
300
350
400
450
500
550